Schweizerische Eidgenossenschaft
Confédération suisse
Confederazione Svizzera
Confederaziun svizra

Federal Department of the Environment, Transport, Energy and Communications DETEC

Swiss Federal Office of Energy SFOE
Energy Research and Cleantech

Final report dated 21.12.2020

EMTR

Novel and efficient algorithms for locating faults in electrical power grids based on an extension of the electromagnetic time reversal theory

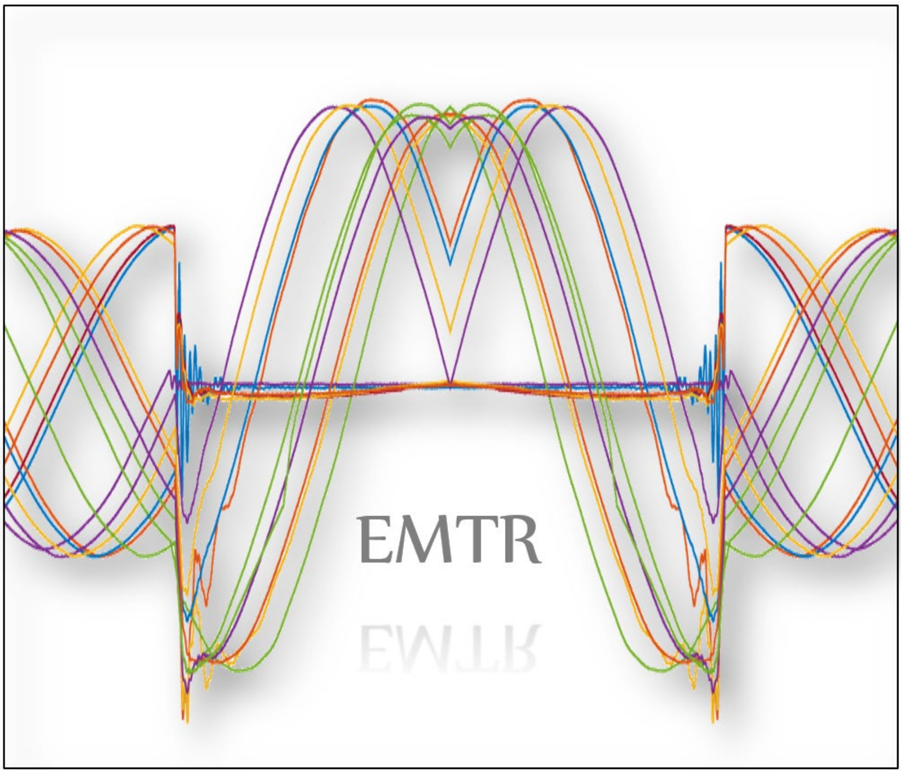

Date: 12.12.2020

Location: Bern

Subsidiser:
Swiss Federal Office of Energy SFOE
Energy Research and Cleantech Section
CH-3003 Bern
www.bfe.admin.ch

Subsidy recipients:
EPFL
EMC Laboratory
EPFL-SCI-STI-FR
Station 11
1015 Lausanne
https://www.epfl.ch/

Streamer International AG
Masanserstrasse 17
7000 Chur
https://www.streamer-electric.ch

Authors:
Dr. Zhaoyang Wang, Ecole Polytechnique Fédérale de Lausanne (EPFL), EMC Laboratory, zhaoyang.wang@epfl.ch
Dr. Hamidreza Karami, Ecole Polytechnique Fédérale de Lausanne (EPFL), EMC Laboratory, hamidreza.karami@epfl.ch
Prof. Farhad Rachidi, Ecole Polytechnique Fédérale de Lausanne (EPFL), EMC Laboratory, farhad.rachidi@epfl.ch
Dr. Asia Codino, Streamer Electric AG, R&D department, asia.codino@streamer-electric.com

SFOE project coordinator:
Dr. Michael Moser, michael.moser@bfe.admin.ch
SFOE contract number: SI/501706-01

Summary

The objective of the research project is to develop an enhanced fault location algorithm based on the electromagnetic time reversal (EMTR) theory. The classical time reversal method requires numerous simulations varying the positions of the fault along the network. In this project, we propose to make use of the concept of time reversal in mismatched media with the objective of getting rid of the multiple simulations needed in the classical method. The objective being ultimately to be able to locate the fault with only one simulation.

The main outcome of the project is therefore the development of novel fault location metrics with improved performance in terms of computation time and fault location accuracy. The performance characteristics of the developed metrics are tested versus numerical simulations. We also present the development of an embedded controller-based fault location system addressing the demand of efficiently implementing EMTR-based fault location metrics in power systems by a suitable hardware platform coupled with proper sensing and triggering units. With the purpose of validating the developed fault location device implementing the proposed fault location metrics, a live pilot test was performed in a medium-voltage distribution feeder where realistic fault occurrences were emulated. Furthermore, a simulation study was carried out to examine the fault location accuracy of EMTR metrics in particular with reference to the impact of incomplete knowledge of power network parameters. Lastly, we propose a method to optimally select the observation point for a given power network in order to ensure maximum efficiency and full observability of the network.

Résumé

L'objectif de ce projet de recherche est de développer un algorithme amélioré de localisation des défauts basé sur la théorie du retournement temporel électromagnétique (EMTR). La méthode classique du retournement temporel nécessite de nombreuses simulations variant la position du défaut le long du réseau. Dans ce projet, nous proposons d'utiliser le concept de retournement temporel dans des milieux dépareillés (mismatched time reversal) avec l'objectif de s'affranchir des multiples simulations nécessaires à la méthode classique. L'objectif étant à terme de pouvoir localiser le défaut avec une seule simulation. Le principal but du projet est donc le développement de nouvelles métriques de localisation des défauts avec des performances améliorées en termes de temps de calcul et de précision de localisation. Les performances des métriques développées sont testées en utilisant des simulations numériques. Nous présentons également le développement d'un système de localisation de défauts basé sur un contrôleur intégré permettant une mise en œuvre efficace de la méthode EMTR. Dans le but de valider le dispositif de localisation de défaut développé, un test pilote a été effectué sur un réseau de distribution moyenne tension où des défauts réalistes ont été émulées. Par ailleurs, la précision de localisation des défauts de la méthode EMTR a été examinée en tenant compte notamment de l'impact d'une connaissance incomplète des paramètres du réseau électrique. Enfin, nous proposons une méthode pour sélectionner de manière optimale le point d'observation pour un réseau électrique donné afin d'assurer une efficacité maximale et une observabilité totale du réseau.

Contents

Abbreviations

DORT	Decomposition of the Time Reversal Operator
EMTR	Electromagnetic Time Reversal
MCCS	Maximum of Cross-Correlation Sequence
MSE	Mean Squared Error
TR-MUSIC	Time Reversal Multiple Signal Decomposition

1 Introduction

1.1 Objective of the Project

The objective of our research project is to develop an enhanced fault location algorithm based on the electromagnetic time reversal theory. The classical time reversal method requires numerous simulations varying the positions of the fault along the network. In this project, we propose to make use of the concept of time reversal in mismatched media with the objective of getting rid of the multiple simulations needed in the classical method. The objective being ultimately to be able to locate the fault with only one simulation. The main outcome of the project will be therefore the development of a novel fault location algorithm with improved performance in terms of computation time and fault location accuracy. The performance characteristics of the developed method will be tested versus numerical simulations and experimental measurements obtained on real distribution networks.

The fault location functionality is an important on-line process required by power systems operation. In the context of distribution networks with the presence of embedded generation, current methods used for detecting and locating faults either suffer from inapplicability or they require multiple time-synchronized sensors to achieve acceptable location accuracies.

Recently, the Electromagnetic Time Reversal (EMTR) has been successfully applied to the problem of fault location of power grids. Compared to existing techniques, the EMTR-based method presents a number of advantages such as its applicability to inhomogeneous and complex networks as well as to DC networks, its robustness against type and impedance of the fault, presence of noise and limited observation time window, and most importantly the use of a single observation point. However, the conventional EMTR-based method requires numerous back-propagation simulations to identify the fault location, since it requires that the medium in the time-reversed phase matches the one in the direct time.

The aim of this project is twofold. First, to derive and exploit the properties of the electromagnetic time reversal in mismatched media in order to improve the fault location algorithm and reduce the computational burden. The issue of the optimal placement of the observation point will also be dealt with in order to ensure the method’s maximum efficiency and the observability of the whole network. It is expected that the number of simulation runs in the time-reversed phase be significantly reduced. Second, to carry out a quantitative evaluation of the performances of the EMTR method, in terms of detection efficiency and location accuracy, and in particular assess the impact of incomplete knowledge of the network parameters.

1.2 Content of the Report

This report synthesizes the research findings achieved in the project carried out in 2019 and 2020. The investigations within Work Package 1, which concerns the properties of mismatched electromagnetic time reversal in an electrical network are presented in Section 2. Furthermore, we report in Section 7 a method to optimally select the observation point for a given network in order to ensure maximum efficiency and full observability of the network. These two points are within the Deliverable D1.1. Within the framework of Work Package 2, a prototype of a fault location device is developed and introduced in Section 4 in terms of its architecture as well as block functions. A pilot test that utilizes the fault location device to deal with realistic fault events in a live distribution feeder is also reported in Section 4 (Deliverable D3.2). In Sections 3 and 5, we present the mathematical proof as well as the respective results of the experimental and numerical validation of the proposed fault location metrics (Deliverable D3.1). Section 6 is devoted to the performance analysis of the proposed metric with respect to the classical metric based on the energy of the fault current signal (Deliverable D4.1). An outlook for future research works is introduced in Section 8.

2 Properties of mismatched time reversal technique

2.1 Time Reversal Focusing Property in Mismatched Media

In this sub-section, we present an experimental study on the focusing property of electromagnetic time reversal (EMTR) in a scattering medium, in particular when moderate lumped mismatch between the forward-phase and backward-phase media occurs. The considered setup consists of a 26×17.5 cm^2 area, in which twenty plexiglass dielectric rods (1-m long and 1-cm diameter) were evenly disposed in a matrix of 4×5 with a separation distance between two adjacent rods being 6.5 cm. The objective is to assess the time-reversal focusing property when a limited number of rods are removed from the medium in the backward stage. The study is complemented by numerical simulations. A time-domain analysis is first performed by simulating the mismatched media cases in the CST- Microwave Studio environment, in a frequency range of 3 to 5 GHz. The transmitting and receiving antennas were modelled using dipole antennas. It is shown that despite moderate lumped mismatch between forward-phase and backward-phase media, the EMTR focusing property remains unimpaired. The focusing property of EMTR in the considered cases of mismatched media is also investigated experimentally in the frequency domain using a Vector Network Analyzer (VNA), in the frequency range from 7 to 18 GHz. The experimental analysis confirms that in absence of one or two rods in the backward phase, the source location could still be identified using the time-reversal technique. The focusing performance was found to be lower than that achieved in matched media.

2.1.1 Introduction

Most laws of nature feature invariance under time reversal (TR), either in the strict or in the soft sense [1], which enables a wide range of applications of TR in different fields of engineering (e.g.,[1]). Particularly, time reversal has been proven to be a powerful technique to focus electromagnetic waves in complex and heterogeneous media. The focusing process using TR is a two-step approach: (i) a diverging signal (e.g., electromagnetic waves) originated by a source (and distorted in an inhomogeneous medium) is captured by receivers, and (ii) the captured signals are time-reversed and synchronously back-injected through the same medium. As a result, the back-propagated signals are refocused to the initial source location.

Note that in typical applications of TR, it is required that the back-propagation medium (i.e., reversed-time medium) is strictly identical to the direct-time medium. However, this may not be the case in some applications related, for instance, to medical care or aerial communication (e.g., [2],[3]) where changes in the medium are inevitable. Also, when locating faults in power networks, since the location of the transverse branch representing the fault is unknown, multiple simulation runs are needed to locate the fault [1]. Consequently, recent research work has been oriented to examining the TR refocusing property when there is a mismatch between the media considered in steps (i) and (ii) described above [4],[5],[6].

Liu *et al.* [6] designed an experimental setup consisting of a number of movable dielectric rods and used it to experimentally study the focusing property of electromagnetic time reversal (EMTR) in a highly scattering environment and, in particular, when the medium changes in the direct time (i.e., forward phase) and reversed time (i.e., backward phase). The refocusing quality was examined in controlled mismatched media by precisely shifting the scatters in the backward phase. Liu *et al.* [6] also studied various techniques for the case in which the media employed in the forward phase is either totally or partially unknown.

In this report, we present a study, inspired by Liu *et al.* [6], investigating the EMTR focusing property in a scattering medium in which moderate lumped changes are applied in the reversed-time phase.

2.1.2 Proposed Setup for the Analysis of the Time-Reversal Focusing Property in Mismatched Media

In [6], Liu *et al.* designed an experimental setup consisting of a number of movable dielectric rods, as shown in Fig. 1. A total of 750 rods were randomly embedded in a 1.2-m long and 2.4-m wide styrofoam baseboard. Two Vivaldi antennas located in a plane bisecting the mid-point of the rods were used as transmitting and receiving antennas over the 0.5 - 10.5 GHz band.

The experiment was performed using the following procedures:

Step 1: In the forward phase, the transmitting antenna (Antenna 1 in Fig. 2.1) generates an electromagnetic wave signal, which propagates through the medium and is received by the receiving antenna (Antenna 2 in Fig. 2.1).

Step 2: In the backward phase, the received signal was time reversed and back emitted by Antenna 2 into either the original medium, which we call matched medium to indicate that it is the same as the forward-phase medium, or a mismatched medium in which the styroform holding the rods was incrementally shifted (in the order of one centimeter) along one direction.

They showed that the time-reversal imaging degrades with increasing media mismatch, and they proposed techniques to alleviate the degradation and make it possible to locate the source.

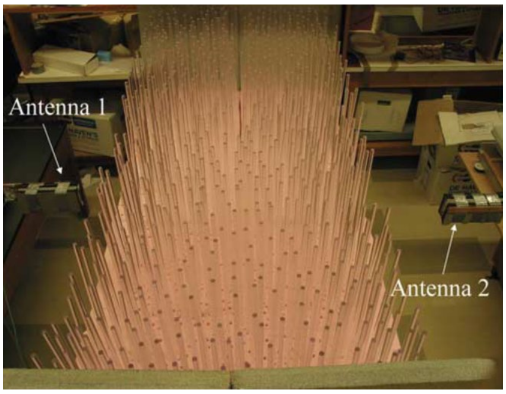

Fig. 2.1. The experimental setup used by Liu et al. [6],. Figure adapted from [6],.

We propose to consider a setup inspired by the work of Liu *et al.* [6], namely a medium containing a number of rods located between the transmitting and receiving antennas. However, unlike [6], the type of mismatch we consider in this study corresponds to lumped changes. The objective is to assess the time-reversal focusing property when a limited number of rods (1 or 2 out of 20) are removed from the medium in the backward stage. As discussed in [7], we hypothesize that a moderate lumped mismatch between the direct-time and reversed-time media would not impair the TR focusing property and the contributions associated with the fixed rods would still enable locating the source.

Unlike the experiment in [6] which employed dielectric rods in large quantities and in an irregular pattern, we considered a simpler setup containing 20 rods arranged in a regular manner between the transmitting and receiving antennas, as illustrated in Figs. 2.2a and 2.2b.

The setup was realized in the EMC Laboratory of the Amir Kabir University of Technology. It consists of a 26×17.5 cm^2 area, in which twenty plexiglass dielectric rods (1-m long and 1-cm diameter) were evenly disposed in a matrix of 4×5 with a separation distance between two adjacent rods being 6.5 cm. Each rod was labelled with coordinates (*r*,*c*) according to the row and column number corresponding to its location (see Fig. 2.2b). The geometrical and electrical parameters of the setup are reported in Table 2.1.

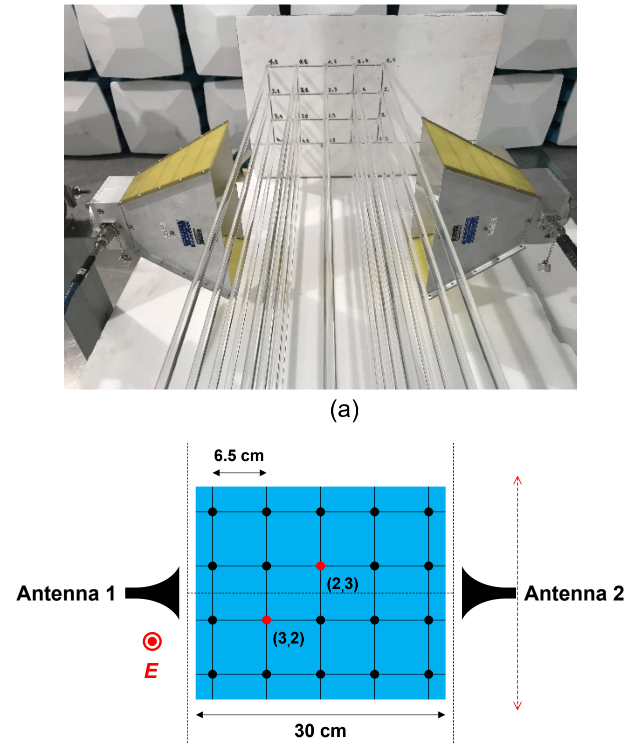

(b)

Fig. 2.2 The proposed experimental setup. (a) Picture of the setup realized in the EMC Laboratory of Amir Kabir University of Technology. (b) Schematic representation of the half-length cross-section of the rods

Table 2.1 The Geometrical and Electrical Parameters of the Setup of Fig. 2.2

Component	Parameter	Value
Rod	Length	1 m
	Diameter	1 cm
	Relative dielectric constant (ε_r) (methyl methacrylate)	2.7
Baseboard	Relative dielectric constant (ε_r) (expanded polystyrene)	2.0

Two double-ridged horn antennas separated by a distance of 30 cm were used as transmitting and receiving antennas. The center point of the transmitting/receiving antenna's aperture is aligned with the half-length cross-section of the rods. Antenna 2 (i.e., the receiving antenna) was mounted on a stepper motor and could thus be moved vertically with a precision of one centimeter. In the forward phase, the electric field was measured by the receiving antenna in the presence of all 20 rods.

In the time-reversed backward stage, we considered the following 4 cases (summarized in Table 2.2):

Case 0: The time-reversed backward medium matches the direct-time medium (no rods removed).

Cases 1 and 2: One rod out of 20 is removed in the backward stage (either (2,3) or (3,2), see Fig. 2.2b).

Case 3: Two rods out of 20 ((2,3) and (3,2), see Fig. 2.2b) are removed in the backward stage.

Table 2.2 Considered Cases for the Time-Reversed Backward Medium

Case n^o		Rod(s) removed in the backward stage
0	Matched	None
1	Mismatched	(2,3)
2	Mismatched	(3,2)
3	Mismatched	(2,3) and (3,2)

In what follows, the EMTR-based focusing capability in the proposed mismatched media will be first investigated using time domain numerical simulations by modelling the setup in the CST-Microwave Studio simulation environment. Then, the experimental results in the frequency domain will be reported.

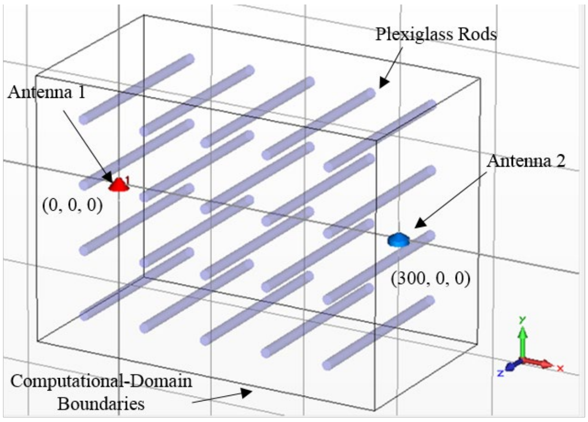

Fig. 2.3. The CST simulation model (for the forward phase) of the experimental setup.

2.1.3 Time-domain Analysis: CST Simulations

As shown in Fig. 2.3, a model of the designed experimental setup (Fig. 2.2) was built in the CST-MWS environment. For the time-domain analysis, a modulated-Gaussian pulse was used to feed the transmitting antenna (Antenna 1). In the simulation study, we used the time-reversal maximum amplitude metric (e.g., [8], [9], and [10]) to assess the focusing performance of EMTR for the matched media (case 0) and for one of the mismatched media cases (case 3). In the CST simulations, the finite integration technique (FIT) transient solver was used.

The simulations served to carry out qualitative studies, and thus, moderate simplifications and modifications were applied in modelling the proposed setup without loss of generality.

The coordinate system was selected in such a way that the half-length cross-section of the rods was aligned with the z = 0 plane, as shown in Fig. 2.3. CST built-in dipole antennas were used as transmitting and receiving antennas. The transmitting and receiving antennas were located along the x-axis with x-y-z coordinates (0, 0, 0) and (300 mm, 0, 0), respectively.

Considering the computation burden, we confined the frequency range of the simulations to the 3-5 GHz frequency range. In view of this, the antennas were tuned for a center frequency of 4 GHz with about 760 MHz bandwidth. Meanwhile, the relative permittivity of the dielectric rod was increased to 3.6 to enhance its scattering effect in the considered frequency band. Furthermore, by virtue of the symmetry in the setup, only the positive z-axis half segment of the rods was considered in the simulations.

The transmitting antenna was vertically polarized and the used modulated-Gaussian pulse, depicted in Fig. 2.4, was generated through the CST built-in function.

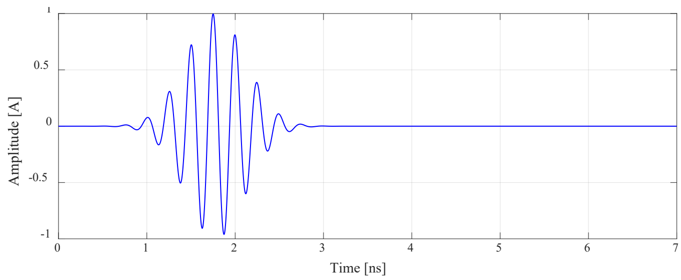

Fig. 2.4 The modulated-Gaussian pulse used as a current source to feed the transmitting antenna in the forward phase.

After the forward-phase computation, the current signal at the output of the receiving antenna (Antenna 2) was time-reversed and normalized with respect to the absolute value of its maximum amplitude, as shown in Fig. 2.5.

The reversed-time signal shown in Fig. 2.5 was back-injected into Antenna 2, which acted as the transmitting antenna in the backward phase, and the output signal received by Antenna 1 was evaluated.

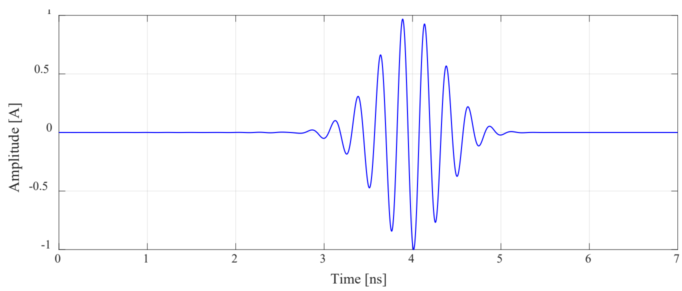

Fig. 2.5 The normalized and time-reversed current of the receiving antenna in the forward phase.

In the simulations with frequencies up to 5 GHz, the target detecting resolution was about 30 mm (l/2). Provided this, three observation points were considered, namely the original source coordinate (0, 0, 0) and two other locations in which the antenna was moved along the positive *y*-axis, respectively, to positions (0, +30 mm, 0) and (0, +60 mm, 0).

Case 0: Matched Media

Fig. 2.6 shows the received signal at the output of Antenna 1 that resulted from the back-injection of the time-reversed signal at the input of Antenna 2. In this case, the backward medium matches the forward one (Case 0). As can be seen in the expanded view (Fig. 2.6b), the current observed at the original source location features the highest amplitude.

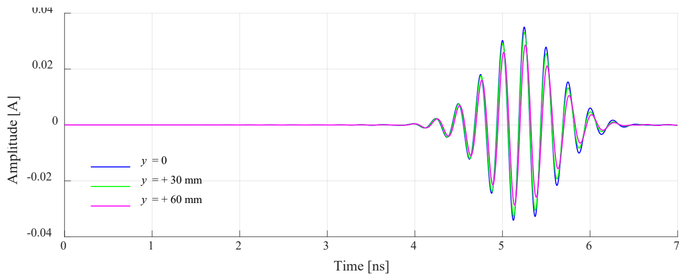

(a)

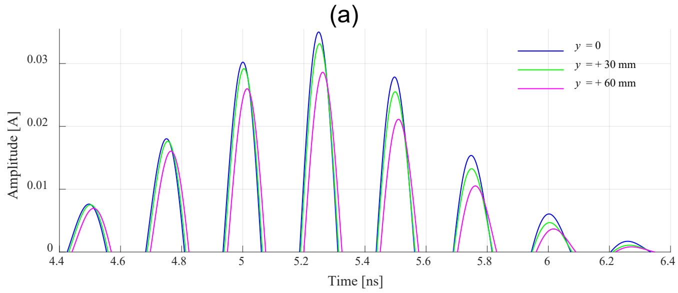

(b)

Fig. 2.6 The current at the output of Antenna 1 resulted from the back-injection of the time-reversed signal at the input of Antenna 2. Three different locations for Antenna 1 were considered: y = 0, corresponding to the exact location of the original source, y = +30 mm and y = +60 mm. (a) Overall waveform. (b) Expanded view. Case 0 (matched media)

Case 3: Mismatched Media

In the mismatched media case, rods (2,3) and (3,2) were removed from the medium in the time-reversed backward phase. As shown in Fig. 2.7, the highest amplitude of the received signal was still obtained at the original location of the source (y = 0). Note that we have not rigorously shown that this point corresponds to the most intense focusing in the whole region of interest. This will be shown in the next Section. Interestingly, the TR focusing property holds even in the presence of moderate lumped mismatch between the direct and reverse media.

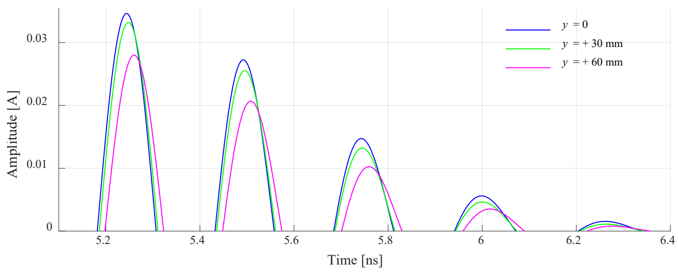

Fig. 2.7 Case 3 (mismatched media: rods (2,3) and (3,2) removed in the backward phase). The plot shows the current at the output of Antenna 1 resulted from the back-injection of the time-reversed signal at the input o Antenna 2. Three different locations for Antenna 1 were considered (y = 0, corresponding to the exact location o the original source, y = +30 mm and y = +60 mm).

2.1.4 Frequency-domain Analysis: Experiments

The focusing property of EMTR in the considered cases of mismatched media was investigated experimentally in the frequency domain using a Vector Network Analyzer (VNA).

As shown in Fig. 2.8, two double-ridged horn antennas separated by a distance of 30 cm were used as transmitting and receiving antennas. Antenna 1 was oriented to generate a vertically-polarized electric field. The transmitting-receiving characteristics were obtained by measuring the S-parameter S21 (transmission coefficient). To this end, a Rohde & Schwarz™ – ZVK type 10Hz – 40 GHz VNA was used. Compared with the numerical simulations, the experimental study was carried out over a higher frequency range, namely 7 to 18 GHz, to intensify the interaction of the propagated fields with the rods.

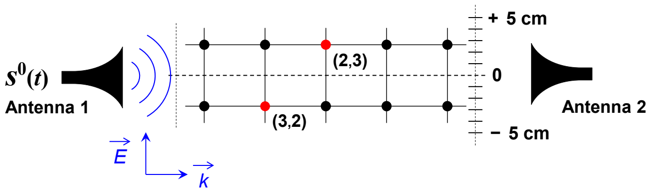

Fig. 2.8 The experimental setup for measuring Antenna 1-2 transmitting-receiving characteristics in the frequency domain.

To facilitate the description, we refer to the measured S21-parameter as a transfer function:

$$T_{n^o}^{0,h}(f) = S21_{n^o}^{h}(f) \tag{2.1}$$

where h in the superscript refers to the height of the receiving antenna (Antenna 2) which was varied from −5 cm to +5 cm:

$$h = -5, -4, \ldots, 0, \ldots, 4, 5,$$

and where 0 in the superscript refers to the height of the transmitting antenna, which is fixed at $h = 0$ (reference height). The subscript n^o corresponds to the 4 cases determined in Table 2, and it takes the following values:

$$n^o = 0, 1, 2, 3.$$

For example, $T_0^{0,-1}$ corresponds to the S21-parameter measured by the VNA when Antenna 2 is at the height of −1 cm with all the rods being present (matched media). The measured magnitude spectrum of $T_0^{0,-1}$ is shown in Fig. 2.5.

Considering the 4 cases of Table 2 and 11 considered heights for Antenna 2, a total of 44 transfer functions were measured in the frequency range of 7 to 18 GHz. In the following analysis, we assume that the initial exciting signal $s^0(t)$ is a Morlet wavelet (see Fig. 10a), given by:

$$s^0(t) = \cos(2\pi f_c \cdot t) \cdot \exp\left[-\left(t/\sqrt{2}\delta\right)^2\right] \tag{2.2}$$

With

$$\delta = 1/f_c \tag{2.3}$$

where f_c is the center frequency of its Gaussian shaped magnitude spectrum, as shown in Fig. 2.10b, assumed to be 12.5 GHz according to the considered 7-18 GHz frequency band.

The forward-phase (direct-time) transfer function in which both antennas are at height $h = 0$ is given by

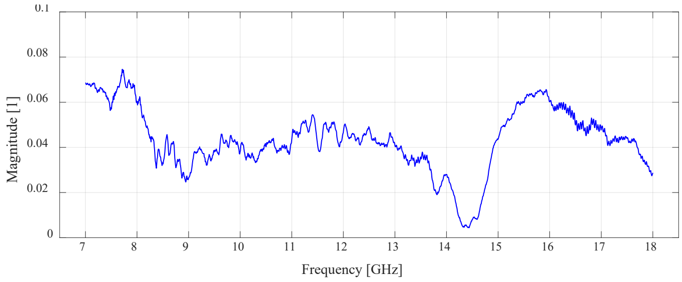

Fig. 2.9 The magnitude spectrum of the measured transfer function $T_0^{0,-1}$.

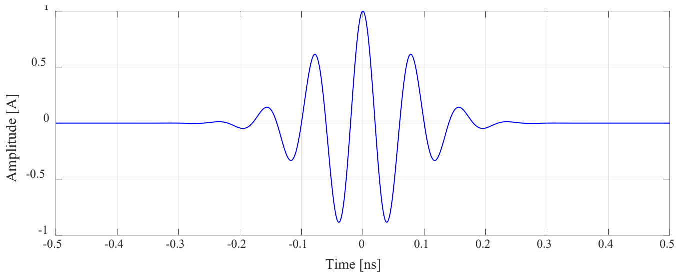

(a)

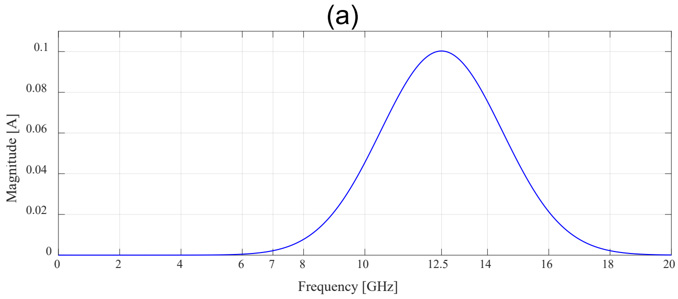

(b)

Fig. 2.10 The Morlet wavelet used as an exciting signal at the input of Antenna 1 in Fig. 2.8. (a) Time-domain waveform. (b) Magnitude spectrum.

$$T^{\mathrm{DT}}(f) = T_0^{0,0}(f) = S21_0^0(f) \tag{2.4}$$

The received signal spectrum $S^{\mathrm{DT}}(f)$ can be expressed as

$$S^{\mathrm{DT}}(f) = T^{\mathrm{DT}}(f) \cdot S^0(f) \tag{2.5}$$

where, $S^0(f)$ is the Fourier transform of $s^0(t)$ feeding Antenna 1 in the forward phase.

The time-reversal operation in the frequency domain corresponds to the complex conjugate transformation of $S^{\mathrm{DT}}(f)$:

$$S^{\mathrm{DT}*}(f) = \left[S^{\mathrm{DT}}(f)\right]^* \tag{2.6}$$

This time-reversed signal was applied to Antenna 2 and transmitted back into the varied medium situations, as depicted in Fig. 2.11.

The frequency spectrum of the signal measured by Antenna 1 in the backward phase can be determined by

$$S_{n^o}^{\mathrm{RT}}(f,h) = S^{\mathrm{DT}*}(f) \cdot T_{n^o}^{0,h}(f) \tag{2.7}$$

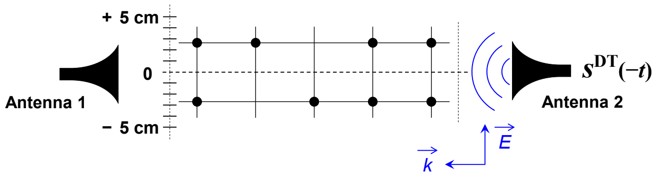

Fig. 2.11 Schematic representation of the backward transmitting-receiving setup (mismatched media case 3).

where n^o corresponds to the considered case (see Table 2.2), and h is the height of the receiving antenna (Antenna 1), as defined earlier.

Case 0: Matched Media

Because of the low-loss medium, the received signal measured at the original source location (i.e., h = 0) is approximately a time-reversed copy of the source waveform [11], [12]. Thus, the source location (specified in this case by a height of Antenna 1 h = 0) can be identified in the frequency domain by using the mean square error between the source waveform and the received signal in the time-reversed backward phase:

$$h^0 = \arg\Big|_h \; min\left\{ MSE(f,h) = \frac{1}{N} \cdot \sum_{f_{lower}}^{f_{upper}} \left| nor\left[S_{n^o}^{RT*}(f,h) \right] - S^0(f) \right|^2 \right\} \tag{2.8}$$

where h^0 is the estimated source location (height of Antenna 1), and N is the number of samples in the frequency band (f_{lower} = 7 GHz and f_{upper} = 18 GHz), set to 1601 in the experiment. The normalizing operation in Eq. (7), expressed by *nor*[], is defined as

$$nor\left[S_{n^o}^{RT*}(f,h) \right] = S_{n^o}^{RT*}(f,h) \Big/ \left| T_0^{0,0}(f) \right|^2 \tag{2.9}$$

Fig. 2.12 presents the evaluated MSE as a function of the height of the receiving antenna for the case of matched media (case 0). As expected, the minimum MSE corresponds to the location of the source.

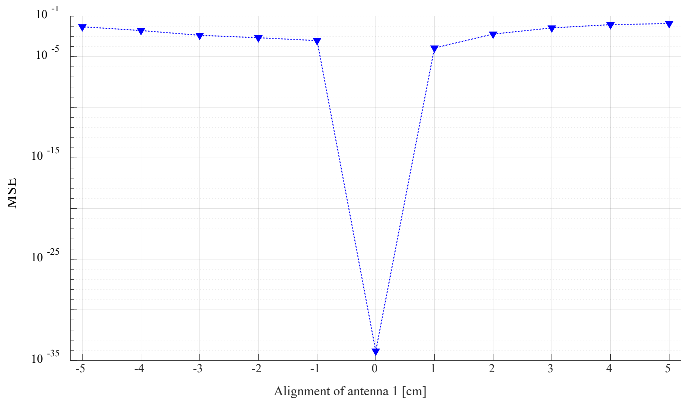

Fig. 2.12 The frequency-domain MSE metric evaluated using Eq. (7) for the case of matched media (Case 0).

Cases 1-3: Mismatched Media

For the three considered mismatched cases defined in Table 2.2, the results of the MSE evaluations are shown in Fig. 2.13. It can be seen that even in the absence of one or two rods in the backward phase, the source location can still be identified using the time-reversal technique. In other words, the moderate lumped mismatch between the forward- and backward-phase media did not impair the TR focusing property. Certainly, the focusing performance is lower than that achieved in matched media (compare Figs. 2.12 and 2.13). However, the contributions associated with the fixed rods still enable locating the source.

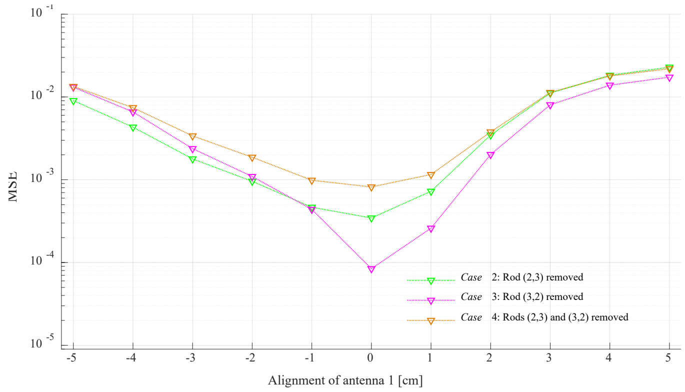

Fig. 2.13 The frequency-domain MSE metric evaluated using Eq. (2.8) for the mismatched media cases 1, 2, and 3.

2.1.5 Summary

We presented a study on the focusing property of electromagnetic time reversal (EMTR) in a scattering medium, in particular when a moderate lumped mismatch between the forward-phase and backward-phase media occurs.

The considered setup consists of a 26×17.5 cm^2 area, in which twenty plexiglass dielectric rods (1-m long and 1-cm diameter) were evenly disposed in a matrix of 4×5 with a separation distance between two adjacent rods of 6.5 cm.

The objective was to assess the time-reversal focusing property when a limited number of rods (1 or 2 out of 20) are removed from the medium in the backward stage.

A time-domain analysis was first performed by simulating the mismatched media cases in the CST Microwave Studio environment, in a frequency range of 3 to 5 GHz. The transmitting and receiving antennas were modelled using dipole antennas. It was shown that despite moderate lumped mismatch between the forward-phase and backward-phase media, the EMTR focusing property remains unimpaired.

Then, the focusing property of EMTR in the considered cases of mismatched media was investigated experimentally in the frequency domain using a Vector Network Analyzer (VNA), in the frequency range from 7 to 18 GHz.

The experimental analysis confirmed that in the absence of one or two rods in the backward phase, the source location could still be identified using the time-reversal technique. The focusing performance was found to be lower than that achieved in matched media. However, the contributions associated with the fixed rods still allowed locating the source.

2.2 Using Electromagnetic Time Reversal in Mismatched Media to Locate Faults in Transmission Lines

The general time-reversal application implies the use of the same propagation medium in the forward- and backward-propagation stages [1]–[4]. In the application of EMTR to fault location, since the true fault location is unknown, the topology of the faulty network changes in the backward-propagation stage, depending on the location of the transverse branch that reproduces a fault occurrence [1], [15]. Inspired by the property of refocusing electromagnetic waves to the original source in lumped mismatched media [16], we extend the classical EMTR-based fault location methods by removing the transverse branch from the faulty power network in the backward-propagation stage.

2.2.1 General Consideration

With regard to the fault location problem, the propagation medium in the fault occurrence stage (i.e., forward-propagation stage) can be described in two main aspects of parameters:

Let us consider the representation of a fault occurrence along a transmission line, as it is illustrated in Fig. 2.14 for the case of a single-wire line above the ground. With regard to the fault location problem, the propagation medium in the fault occurrence stage (i.e., forward-propagation stage) can be described in two main aspects of parameters:

i) physical characteristics of the line, namely its length L, characteristic impedance Z_C and propagation constant γ, and

ii) boundary conditions at the line terminals and the fault location.

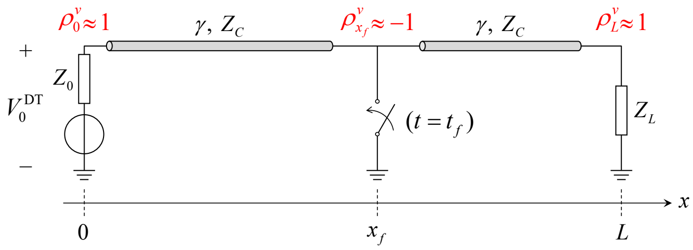

Fig. 2.14 Schematic representation of a fault occurrence in power networks. ρ_0^v, ρ_L^v and $\rho_{x_f}^v$ are the voltage reflection coefficients at the line terminals, $x = 0$ and $x = L$, and the fault location, $x = x_f$, respectively.

The boundary condition is generally quantitatively described by using the voltage (or current) reflection coefficient in the transmission-line theory. The line extremities constitute, to a first approximation, open circuits from the viewpoint of the frequency contents of fault-associated transient signals. As a result, $\rho_0^v \approx +1$ and $\rho_L^v \approx +1$. Conversely, the voltage reflection coefficient associated with the fault location is close to -1 when a solid or low-impedance fault is assumed.

In the classical EMTR-based fault location approaches, a fault occurrence is reproduced in the backward stage, bringing about $\rho_{x_f}^v = -1$, as shown in Fig. 2.15a. Since the true fault location is unknown, a set of *a priori* guessed fault locations are assumed. The time-reversal inherent spatial correlation property allows the true fault location to be uniquely characterized among those guessed fault locations by the maximum amplitude or energy of the fault current signal [10], [15]. For this reason, the classical implementation of EMTR requires numerous independent backward-propagation simulations to estimate the most likely fault location. When a higher location accuracy is desired, the guessed fault locations need to be defined with increasing density. This way, the increasing number of guessed fault locations necessarily calls for increasing computation time.

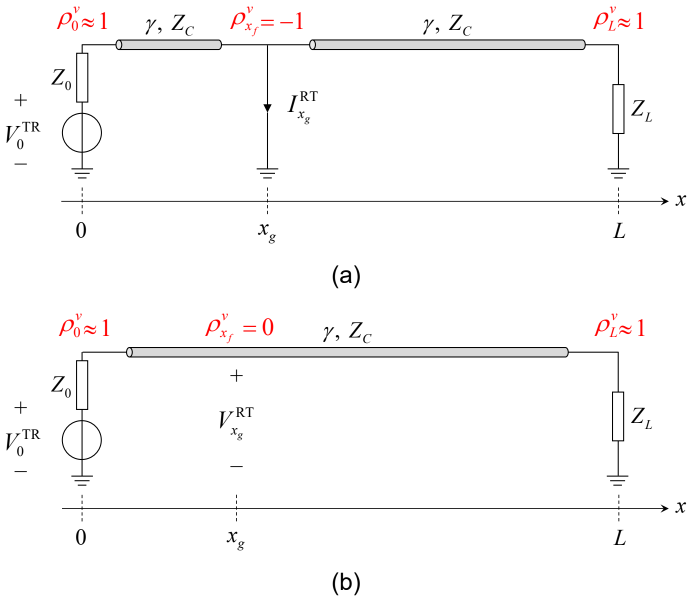

Fig. 2.15 Simplified representation of EMTR applied to locate faults in power networks based on (a) the matched-media condition and (b) the mismatched-media condition.

In view of the above, we propose to consider a fixed topology of a non-faulty power network in the backward-propagation stage, excluding the transverse branch associated with reproducing a fault, as it can be seen in Fig. 2.15b. This would effect a mismatch between the forward-and backward-propagation media as a result of changing the boundary condition at the fault location from the state of fault (i.e., $\rho_{x_f}^v = -1$) to that of non-fault (i.e., $\rho_{x_f}^v = 0$). This also constitutes a lumped mismatch in the sense that all the other line parameters and boundary conditions remain intact.

We hypothesize that the absence of the reflection and transmission processes at the fault location still allows the identification of the fault location. In other words, we assume that the contributions associated with reflections from line terminals (and discontinuities, if any) would suffice to determine the location of the fault. This assumption can be justified by the fact that, in general, two types of components contribute to form the transient signal in response to a fault event:

i) the direct contribution coming from the fault (location) itself, and

ii) the indirect contribution coming from the reflection and transmission processes associated with the line terminals and junctions.

Let us assume to be in a hypothetical fully matched (non-reflective) medium in which the only contribution comes from the fault itself. In this case, the localization of the fault would simply not be possible by back-injecting the time-reversed transients. Thus, to locate the fault using EMTR-based methods, the components associated with the indirect contributions are by far more important than that from the fault itself.

Moreover, the proposed mismatched media also serves the purpose of realizing a faster fault response, since the multiple independent simulations at the guessed fault locations are no longer required in the backward-propagation stage. Specifically, only one simulation run is needed by considering the fixed line-topology without the transverse branch reproducing a fault. Instead of simulating the fault current as it is in the classical implementation of EMTR, the voltage along the line is considered as the characteristic quantity to infer the true fault location.

2.2.2 Transfer Functions in Mismatched Media

For describing the proposed two-stage procedure of applying EMTR in mismatched media to locate faults in transmission-line networks, we first derive the solutions to the following variables in the frequency domain:

i) The analytical expression of the voltage computed at the observation point $x = 0$ in the frequency domain is as follows

$$V_0^{\mathrm{DT}}(j\omega) \triangleq V(x=0, j\omega) = (1+\rho_0^v) \cdot \frac{e^{-\gamma(j\omega)\cdot x_f}}{1+\rho_0^v \cdot e^{-\gamma(j\omega)\cdot 2x_f}} \cdot V_f(j\omega) \quad (2.10)$$

where we consider a homogeneous transmission line of length L, propagation constant $\gamma(j\omega)$, and a fault occurrence at $x = x_f$. ρ_0^v represents the voltage reflection coefficient at the beginning of the line.

ii) The time-reversed voltage response that results from the complex conjugate operation

$$V_0^{\mathrm{DT}}(j\omega) \to V_0^{\mathrm{TR}}(j\omega):\ V_0^{\mathrm{TR}}(j\omega) = \left[V_0^{\mathrm{DT}}(j\omega)\right]^* \quad (2.11)$$

iii) The voltage along the line with an imposed source $V_0^{\mathrm{TR}}(j\omega)$ being applied at the observation point in the backward-propagation stage

$$V^{\mathrm{RT}}(x, j\omega) \triangleq V^{\mathrm{RT}}(x, j\omega) = (1-\rho_0) \cdot \frac{e^{-\gamma(j\omega)\cdot x} + \rho_L^v \cdot e^{\gamma(j\omega)\cdot(2L-x)}}{2\left[1-\rho_0^v \cdot \rho_L^v \cdot e^{-\gamma(j\omega)\cdot 2L}\right]} \cdot V_0^{\mathrm{TR}}(j\omega) \quad (2.12)$$

where ρ_L^v is the voltage reflection coefficient at the end of the line, namely $x = L$.

Next, to relate the above-formulated variables, we first introduce the direct-time transfer function as the ratio of the output function $V_0^{\mathrm{DT}}(j\omega)$ to the input function $V_f(j\omega)$, namely

$$H^{\mathrm{DT}}(x_f, j\omega) = \frac{V_0^{\mathrm{DT}}(j\omega)}{V_f(j\omega)} \quad (2.13)$$

and, we define in a similar way the reversed-time transfer function

$$H^{\mathrm{RT}}(x, j\omega) = \frac{V^{\mathrm{RT}}(x, j\omega)}{V_0^{\mathrm{TR}}(j\omega)} \quad (2.14)$$

It is important to underline that the output function $V_0^{\mathrm{DT}}(j\omega)$ in the direct time is time reversed and then behaves as the input in the reversed time. As a result, we can write

$$V^{\mathrm{RT}}(x, j\omega) = H^{\mathrm{RT}}(x, j\omega) \cdot \left[H^{\mathrm{DT}}(x_f, j\omega)\right]^* \cdot \left[V_f(j\omega)\right]^* \quad (2.15)$$

to relate the output in the reversed time to the input in the direct time.

Finally, we define the direct-reversed-time transfer function as

$$H(x, j\omega) = H^{\mathrm{RT}}(x, j\omega) \cdot \left[H^{\mathrm{DT}}(x_f, j\omega) \right]^* \tag{2.16}$$

that can be analytically expressed as follows:

$$H(x, j\omega) = (1-\rho_0) \cdot \frac{e^{-\gamma(j\omega)\cdot x} + \rho_L^v \cdot e^{\gamma(j\omega)\cdot(2L-x)}}{2\left[1-\rho_0^v \cdot \rho_L^v \cdot e^{-\gamma(j\omega)\cdot 2L}\right]} \cdot \left[(1+\rho_0^v) \cdot \frac{e^{-\gamma(j\omega)\cdot x_f}}{1+\rho_0^v \cdot e^{-\gamma(j\omega)\cdot 2x_f}} \right]^* \tag{2.17}$$

This way, the general task of locating faults in transmission-line networks can be accomplished through investigating the behavior of the direct-reversed-time transfer function as it behaves as a function of the longitudinal coordinate x [17].

3 Proof of Concept through Off-line Simulations and Experimental Validation

3.1 Property: Bounded Phase of the Direct-Reversed-Time Transfer Function

3.1.1 Theorem 1: Bounded Phase of $\boldsymbol{H(x, j\omega)}$

The phase angle of the direct-reversed-time transfer function of EMTR in mismatched media presents the following property.

Theorem 1

$$\text{if } x = x_f,\ \angle H(x_f, j\omega) \in (-\pi/2,\ \pi/2);$$

$$\angle\, x \neq x_f,\ \exists\, f = \omega/2\pi\colon \angle H(x, j\omega) \notin (-\pi/2,\ \pi/2).$$

The symbol of $\angle$ denotes phase angle or argument in radians. The property described by Theorem 1 hereafter is referred to as the bounded phase property. The proof of this theorem can be found in [7].

3.1.2 Numerical Validation

We present the first numerical example to validate the bounded phase property suggested by Theorem 1, making reference to a single-conductor transmission line specified by the per-unit-length parameters of typical 20-kV overhead lines.

The line is assumed to be connected at both ends to power transformers, which are represented by their high-frequency input impedance ($Z_0 = Z_L = 100$ kΩ in this example). The line length L is 6.5 km and the fault is assumed to occur at 3.6 km away from the line terminal $x = 0$, where the observation point is located.

Figure 3.1a shows the computed phase angle of $H(x_g, j\omega)$ for Case *i)* wherein the guessed fault location x_g is exactly the true fault location x_f . As it can be observed, the phase angle of $H(x_f, j\omega)$ is bounded by $\pm\pi/2$, confirming the formulated phase property. The computation involves a frequency range between 100 Hz and 5 MHz, considering a frequency step equal to 10 Hz.

In Cases *ii)* and *iii)*, x_g is assumed to be $x_f + \Delta x$, with Δx being respectively +100 m (see Fig. 3.1b) and −20 m (see Fig. 3.1c). Δx denotes a difference between the guessed fault location x_g and the true fault location x_f . It is evident that, in these two cases, the argument of $H(x_g, j\omega)$ exhibits some out-of-range values at higher frequencies even though it is still bounded by $\pm\pi/2$ at lower frequencies.

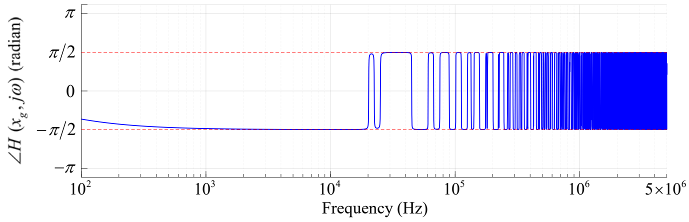

(a)

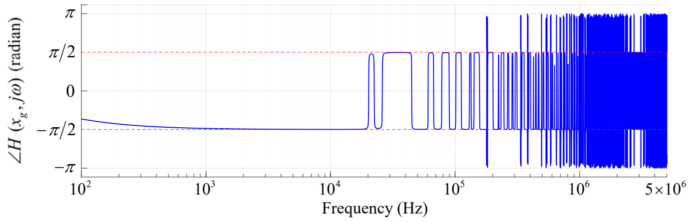

(b)

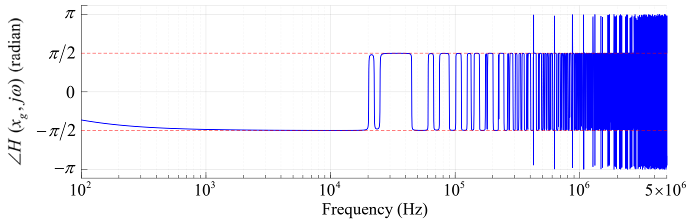

(c)

Fig. 3.1 Phase angle of the transfer function $H(x_g, j\omega)$ for a 20-kV single-conductor overhead line ($L = 6.5$ km, $x_f = 3.6$ km), for (a) $x_g = x_f$, (b) $x_g = x_f + 100$ m, and (c) $x_g = x_f - 20$ m, with f ranging from 100 Hz to 5 MHz and the frequency step being 10 Hz.

The numerical validation is extended to further observe the distribution of $H(x_g, j\omega)$ in the complex plane. As it is suggested in the proof, only if xg coincides with x f is the real part of $H(x_g, j\omega)$ positive. Fig. 3.2 compares the four-quadrant distribution of the complex-valued $H(x_g, j\omega)$ as a function of $\omega = 2\pi \cdot f$ for three cases: *i)* $x_g = x_f$ (i.e., Fig. 3.2a), *ii)* $x_g = x_f + 15$ m (i.e., Fig. 3.2b), and iii) $x_g = x_f - 100$ m (i.e., Fig. 3.2c). f ranges from 100 Hz to 5 MHz and is discretized by an increment of 100 Hz.

As it can be observed, the real and imaginary parts of the normalized transfer function are confined within the region of $[-1, 1] \times [-j,\ j]$ in the complex plane. In particular, for the case of Fig. 3.2a, $(Re\{H(x_g = x_f, j\omega)\}, Im\{H(x_g = x_f, j\omega)\})$ is only located in Quadrants I and II, thus ensuring the phase angle of $H(x_g = x_f, j\omega)$ not being over the limit of $\pm\pi/2$.

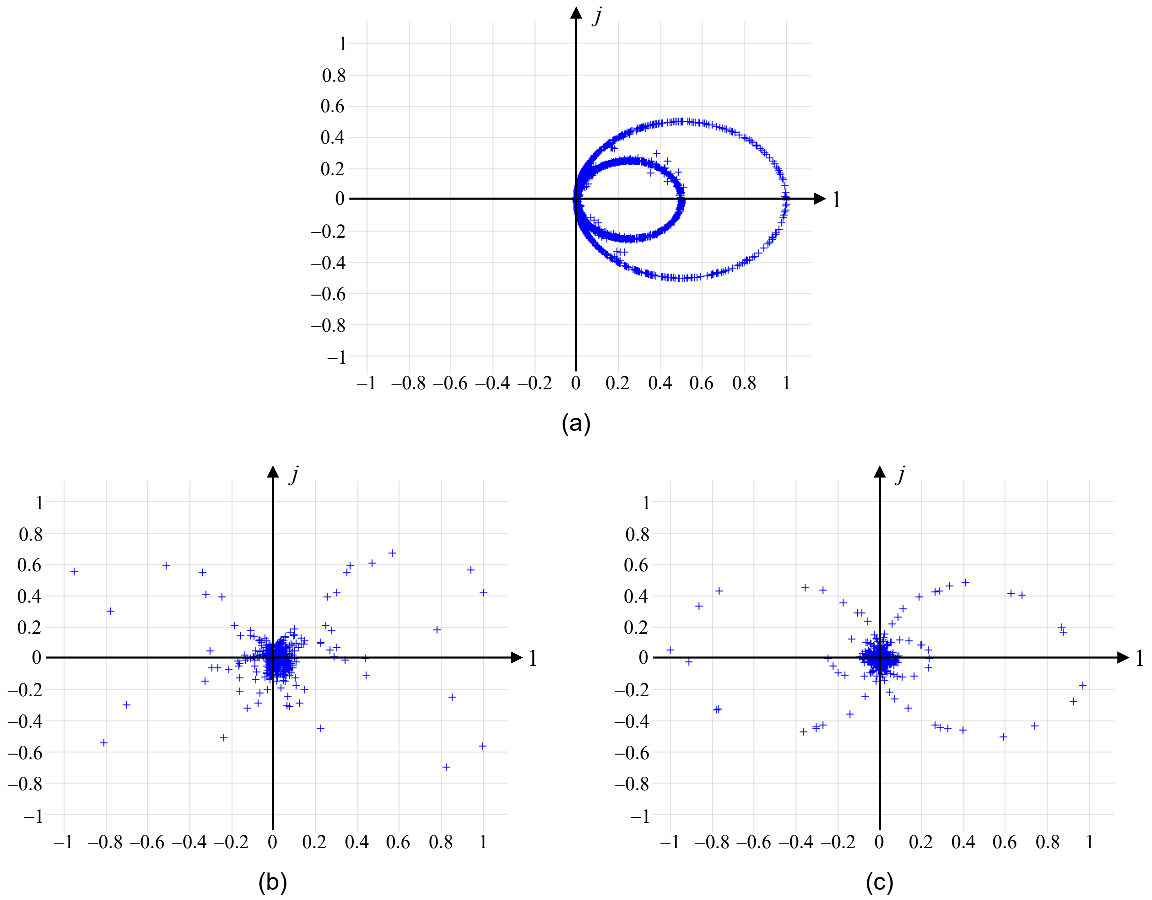

Fig. 3.2 Four-quadrant distribution of the normalized transfer function for a 20-kV single-conductor overhead line ($L = 6.5$ km, $x_f = 3.6$ km), for (a) $x_g = x_f$, (b) $x_g = x_f + 15$ m, and (c) $x_g = x_f - 100$ m, with f ranging from 100 Hz to 5 MHz and the frequency step being 10 Hz.

3.1.3 Application Examples

Although the formulation of Theorem 1 makes reference to a simplified line set-up, namely a non-branched homogeneous overhead line, we show two examples in this section that the proposed bounded phase property is applicable to more topologically-complex networks. To be specific, a single-phase line composed of mixed overhead-coaxial cable lines and a Y-shaped inhomogeneous network are considered. The adopted parameters refer to those of typical line/cables in distribution/transmission networks and the line losses are also taken into account in these simulations.

1) *Single-phase inhomogeneous transmission line*

The first simulation case considers a 20-kV inhomogeneous transmission line with an overall length $L_1 + L_2 = 15$ km, consisting of an overhead line of length $L_1 = 6$ km and a coaxial cable of length $L_2 = 9$ km. The line is terminated at each of the ends with a power transformer, whose high-frequency input impedance is assumed to be 100 kΩ. The line terminal $x = 0$ constitutes the single observation point.

a) *Fault occurrence along the overhead line at $x = x_f = 2.1$ km*

Figure 3.3 illustrates the calculated phase angle of the transfer function $H(x_g, j\omega)$ as a function of the guessed fault location x_g and the frequency f. x_g is defined along both the overhead line and the underground cable with an increment of 100 m. f ranges from 1 kHz to 1 MHz with $\mathrm{d}f$ equaling 100 Hz. For the sake of observation, Fig. 3.3 plots at each x_g only the out-bounded phase angle, namely $\angle H(x_g, j\omega) \notin (-\pi/2,\ \pi/2)$. The true fault location $x_g = x_f$ can be clearly distinguished from the other guessed fault locations. To be specific, x_f exclusively features a bounded phase angle among the guessed fault locations, displaying a null distribution of $\angle H(x_f, j\omega)$ throughout the considered frequency range. That is to say, it confirms that $\angle H(x_f, j\omega)$ is bounded by $\pm\pi/2$.

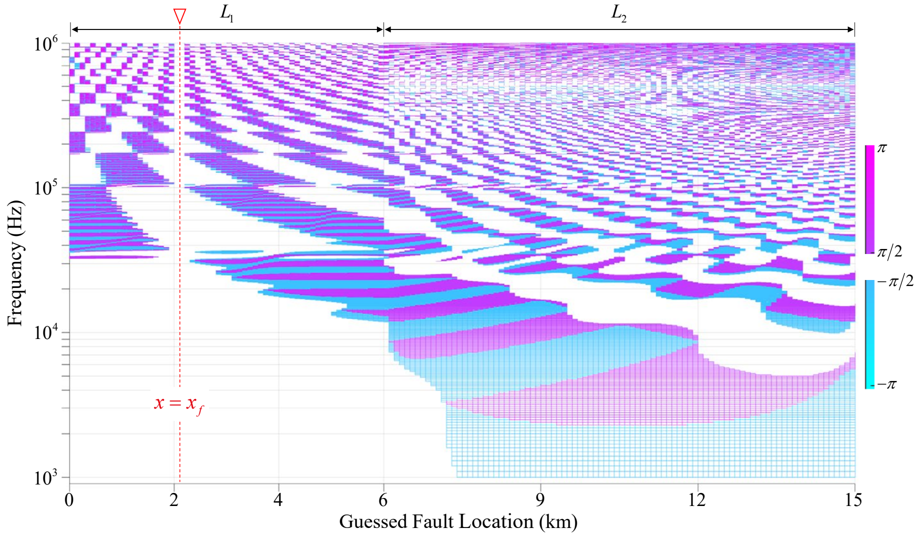

Fig. 3.3 Phase angle of the transfer function $H(x_g, j\omega)$ as a function of the guessed fault location x_g and the frequency f.

***b)** Fault occurrence along the coaxial cable at $x = x_f = 10.8$ km*

We consider now a fault event along the cable section with $x_f = 10.8$ km. Fig. 3.4 shows the phase angle of the transfer function versus frequency for each guessed fault location. Again, it is confirmed that the only location rendering $\angle H(x_g, j\omega)$ bounded appears at the true fault location.

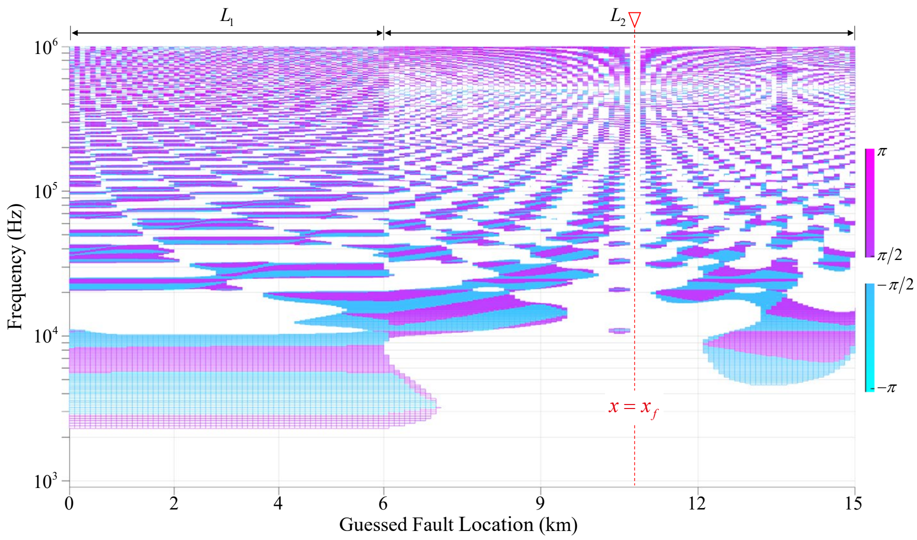

Fig. 3.4 Phase angle of the transfer function $H(x_g, j\omega)$ as a function of the guessed fault location x_g and the frequency f.

2) *Y-Shaped inhomogeneous network*

The applicability of the formulated transfer function property is further discussed by taking account of the topological complexity of transmission-line networks, thereby a Y-shaped network (see Fig. 3.5) is considered to represent generic teed networks that contain an arbitrary number of line branches and nodes. To be specific, the line/cable sections are respectively 6 km ($L_1 = 6$ km), 11 km ($L_2 = 11$ km), and 5 km ($L_3 = 5$ km) in length. To facilitate the description, the three line branches hereafter are referred to by their respective lengths.

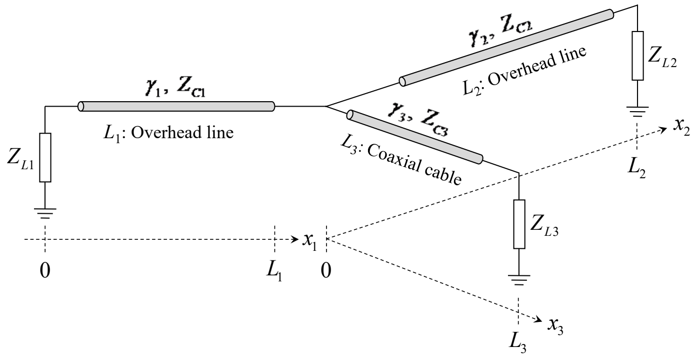

Fig. 3.5 Schematic representation of the Y-shaped inhomogeneous transmission-line network.

The considered Y-shaped network is inhomogeneous. Specifically, Branches L_1 and L_3 correspond respectively to 380-kV overhead line and coaxial cable. To enhance the inhomogeneity of the network, Branch L_2 is modeled with a very different cable model corresponding to a 20-kV overhead line.

We assume that a solid fault occurs at an arbitrary location along the three line branches. Then the transfer function $H(x_g, j\omega)$ is calculated based on the single observation point being separately located at the left end of Branch L_1 (i.e., $x_1 = 0$), the right end of Branch L_2 (i.e., $x_2 = 11$ km) and the right end of Branch L_3 (i.e., $x_2 = 5$ km). The network is grounded at the three ends with the high impedance, showing $Z_{L_1} = Z_{L_2} = Z_{L_3} = 100$ kΩ, to model the input impedance of the terminal transformer.

In what follows, we report the assessment of the bounded phase property in two fault cases:

i) fault occurrence along the 20-kV overhead line (i.e., Branch L_2) at $x_2 = x_f = 7.9$ km, and

ii) fault occurrence along the 380-kV coaxial cable (i.e., Branch L_3) at $x_3 = x_f = 3.7$ km.

a) *Fault occurrence along Branch L_2 at $x_2 = x_f = 7.9$ km*

The three subgraphs in Fig. 3.6 show in the $x_g - f$ plane the calculated and color-coded phase angle of the transfer function $H(x_g, j\omega)$, corresponding to the guessed fault locations being defined along Branches L_1, L_2 and L_3 with a distance step $\mathrm{d}x$ of 100 m. The terminals of the two non-faulty line branches, namely $x_1 = 0$ and $x_3 = 5$ km, are referred to as the far ends relative to defining the terminal of the faulty line branch itself as the near end (i.e., $x_2 = 11$ km).

The presented results in Fig. 3.6 are associated with using the far end $x_1 = 0$ as the single observation point. As it can be seen in Fig. 3.6, in spite of the enhanced topological complexity and inhomogeneity of the network, the proposed transfer function property is still validated, showing that $\angle H(x_g = x_f, j\omega)$ is bounded by $\pm\pi/2$. It is worth noting in Fig. 3.7 that a similar distribution of $\angle H(x_g, j\omega)$ along Branch

L_2 can be obtained when formulating the transfer function based on another far end (e.g., $x_3 = 5$ km) as the observation point.

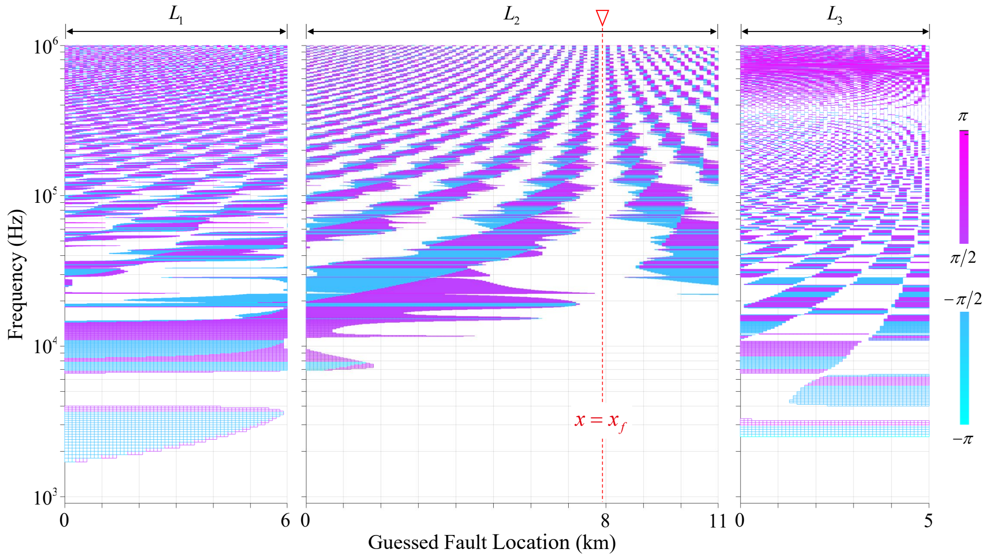

Fig. 3.6 Phase angle of the transfer function based on the far end $x_1 = 0$ as the single observation point.

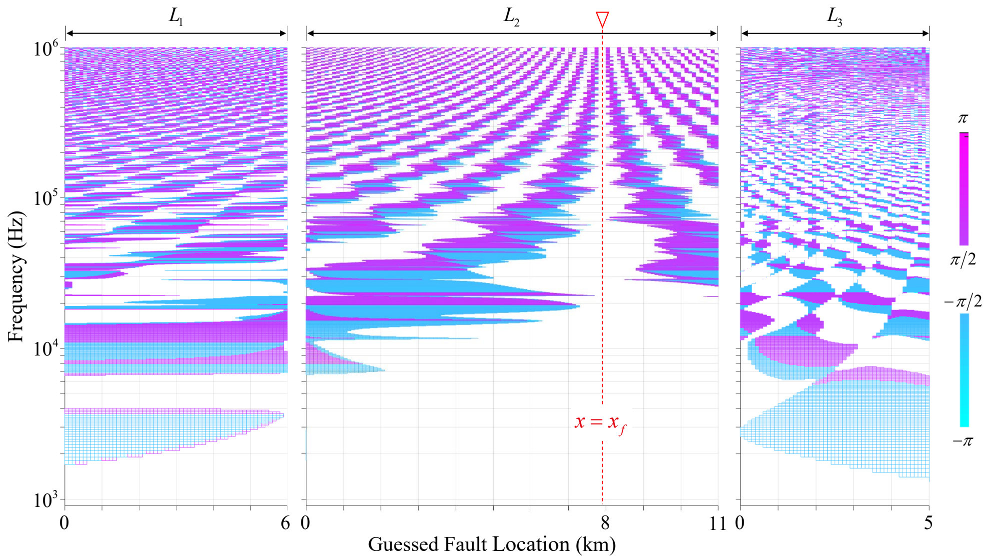

Fig. 3.7 Phase angle of the transfer function based on the far end $x_3 = 5$ km as the single observation point.

b) Fault occurrence along *Branch* L_3 *at* $x_3 = x_f = 3.7$ *km*

The final example assumes a fault occurrence along the coaxial cable L_3 at $x_3 = x_f = 3.7$ km. As discussed earlier, the proposed phase property is independent of the location of the single observation point. Here, we present the calculation resulting from deploying the observation point at the far end $x_2 = 11$ km. As it can be seen in Fig. 3.8, at the true fault location, the transfer function $H(x_g = x_f, j\omega)$ displays the bounded phase angle between $\pm\pi/2$.

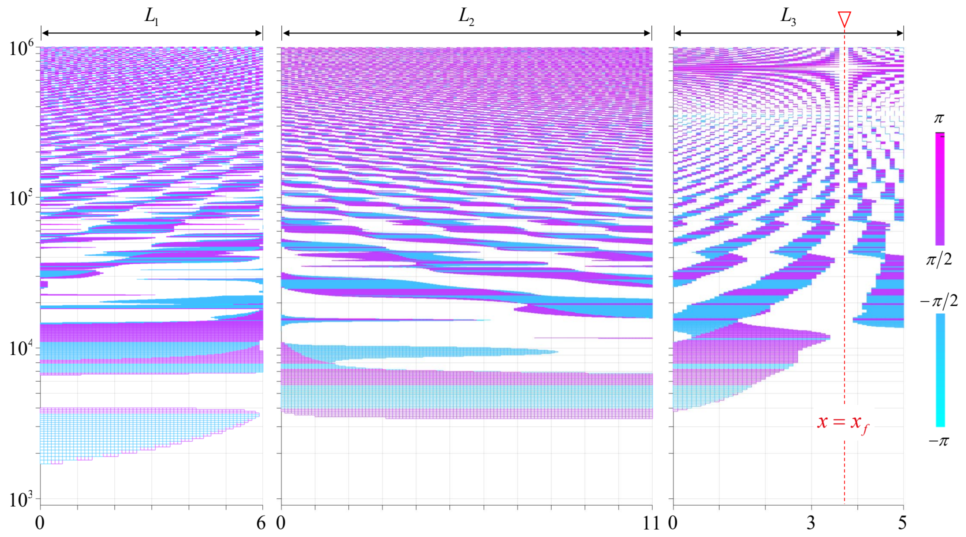

Fig. 3.8 Phase angle of the transfer function based on the far end $x_2 = 11$ km as the single observation point.

3.2 Property: Bounded Phase of the Direct-Reversed-Time Transfer Function

3.2.1 Theorem 2: Mirrored Minimum Squared Modulus of $H(x, j\omega)$

Theorem 2

$$\forall f_i \in \mathbb{F}^{\mathrm{DT}} = \left\{ f_i = (2i-1) \cdot f^0 \middle| f^0 = 1/(4\Gamma_{x_f}),\ \ i = 1, 2, 3, \ldots \right\},$$

$$x_{min} \triangleq \underset{0<x<L}{\mathrm{Min}} \left\{ |H(x, j\omega)|^2 |_{\omega = 2\pi \cdot f} \right\} = L - x_f.$$

$\mathbb{F}^{\mathrm{DT}}$ contains the fault inherent switching frequency and its odd harmonics.

Theorem 2 explains that at every single frequency among $\mathbb{F}^{\mathrm{DT}}$, the squared modulus of $H(x, j\omega)$ reaches its minimum always at the location x_{mirror}, which is the mirror image point of the true fault location x_f with respect to the line center, namely $x_{mirror} = L - x_f$.

3.2.2 Corollary 1 and 2: Mirrored Minimum Energies of $H(x, j\omega)$ and $V^{\mathrm{RT}}(x, j\omega)$

The transfer function constitutes the frequency-domain representation of the unit impulse response of a linear time-invariant system. According to Parseval's theorem, we calculate the energy of the impulse response of the direct-reversed-time system at $\mathbb{F}^{\mathrm{DT}}$ as follows:

$$E\left\{ H\big|_{\mathrm{F^{DT}}} \right\} \triangleq E\left\{ H(x, j\omega)\big|_{\omega = 2\pi \cdot \mathrm{F^{DT}}} \right\} = \sum_{i=1}^{N} \left\{ \left| H(x, j\omega) \right|^2 \Big|_{\omega = 2\pi \cdot \mathrm{F^{DT}}} \right\} \tag{3.1}$$

Corollary 1

$$\exists\ \mathbb{F}^{\mathrm{DT}} = \left\{ f_i = (2i-1) \cdot f^0 \middle| f^0 = 1/(4\Gamma_{x_f}),\ \ i = 1, 2, 3, \ldots \right\},$$

$$x_{min} \triangleq \underset{0<x<L}{\mathrm{Min}} \left\{ E\{ H|_{\mathbb{F}^{\mathrm{DT}}} \} \right\} = L - x_f.$$

Similarly, the energy of the reversed-time voltage $V^{\mathrm{RT}}(x, j\omega)$ can be calculated at $\mathbb{F}^{\mathrm{DT}}$ as:

$$E\left\{V^{\mathrm{RT}}\Big|_{\mathbb{F}^{\mathrm{DT}}}\right\} \triangleq E\left\{V^{\mathrm{RT}}(x,j\omega)\Big|_{\omega=2\pi\cdot\mathbb{F}^{\mathrm{DT}}}\right\} = \sum_{i=1}^{N}\left\{\left|V^{\mathrm{RT}}(x,j\omega)\right|^{2}\Big|_{\omega=2\pi\cdot\mathbb{F}^{\mathrm{DT}}}\right\} \tag{3.2}$$

Corollary 2

$$\exists\ \mathbb{F}^{\mathrm{DT}} = \left\{f_i = (2i-1)\cdot f^0 \middle| f^0 = 1/(4\Gamma_{x_f}),\ \ i = 1,2,3,\ldots\right\},$$

$$x_{min} \triangleq \underset{0<x<L}{\mathrm{Min}} \left\{E\{V^{\mathrm{RT}}|_{\mathbb{F}^{\mathrm{DT}}}\}\right\} = L - x_f.$$

Based on the above-established properties named mirrored minimum squared modulus and energy, the true fault location can be identified by its mirror image point through

$$\begin{aligned} x_f &= L - x_{min} \\ &= L - \underset{0<x<L}{Min}\left\{E\left\{H\big|_{\mathbb{F}^{\mathrm{DT}}}\right\}\right\} \\ &= L - \underset{0<x<L}{Min}\left\{E\left\{V^{\mathrm{RT}}\big|_{\mathbb{F}^{\mathrm{DT}}}\right\}\right\} \end{aligned} \tag{3.3}$$

The proof of Theorem 2 and its two corollaries are given in [18].

3.2.3 Numerical Validation

In this section, we numerically illustrate the properties stated in Theorem 2 and its two corollaries. To this end, an 11-km-long single-phase overhead line of the 380-kV per-unit-length parameters is considered. At the line terminals, the high-frequency input impedance is assigned 100 kΩ. The single observation point is located at $x = 0$. The fault occurrence is assumed to be at $x = x_f = 7$ km.

We first observe the squared modulus of $H(x_g, j\omega)$ in Fig. 3.9a as a function of the guessed fault location x_g together with the order of harmonics $2i - 1$. For defining the values of the former independent variable x_g, the 11-km-long line is discretized by an increment step of 10 m. As to the latter one, we consider the maximum value of i as 20 to include f_0 and its odd harmonics up to the 39-th order. f_0 is 10.4 kHz for the fault case. For the sake of comparison, at each harmonic, the calculated squared moduli at the guessed fault locations are normalized with reference to the global maximum.

As it is shown in Fig. 3.9a, in agreement with Theorem 2, the mirror image point $x_g = L - x_f = 4$ km is indicated at each harmonic by the color signifying the minimum squared modulus of $H(x_g, j\omega)$. Fig. 3.9b presents a finer observation of the behavior of $H(x_g, j\omega)$ at the locations adjacent to the mirror image point $x = L - x_f$. The discretization step is reduced to 1 m to define the guessed fault locations in the spacing between $x = 4$ km ± 100 m. It confirms, on a meter scale, that the mirror image point uniquely features the property of Theorem 2.

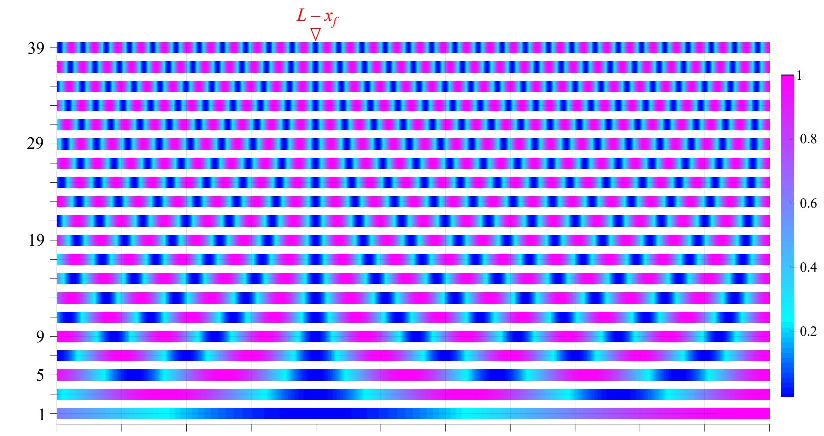

(a)

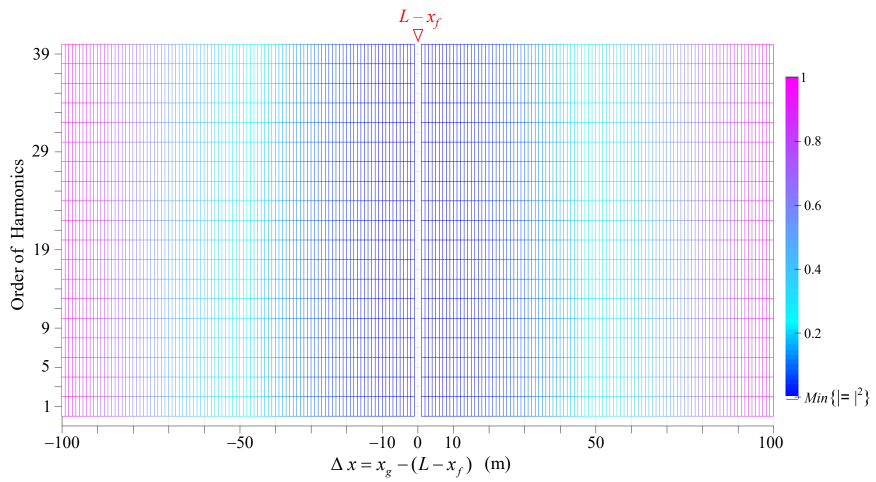

(b)

Fig. 3.9 Normalized squared modulus of $H(x_g, j\omega)$ calculated at f_0 and its odd harmonics up to the 39-th order. The line length L is 11 km and the fault location is $x_f = 7$ km. The guessed fault locations are defined: (a) every 10 m along the line and (b) every 1 m in the spacing between $(L - x_f) \pm 100$ m.

Figure 3.10 presents the calculated energy of the direct-reversed-time transfer function. The curves of $E\{H|_{\mathbb{F}\mathrm{DT}}\}$ versus x_g shown in the subgraphs respectively result from summating $\left|H(x_g, j\omega = j2\pi \cdot f_i)\right|^2$ for f_i up to the first 2, 10, and 20 order odd harmonics. Note that the normalization results in the calculated maximum energy at the unit value. In all the three scenarios, $E\{H|_{\mathbb{F}\mathrm{DT}}\}$ reaches its minimum at $x_g = 4$ km, which is the mirror-image point of the true fault location.

Additionally, as it is in the previous analysis, the guessed fault locations are defined at the neighboring locations of $x_g = L - x_f$ with a finer distance increment ($\mathrm{d}x = 1$ m) to examine the property on a meter scale. As it can be observed in each subgraph on the right the minimum energy remains at the mirror image point.

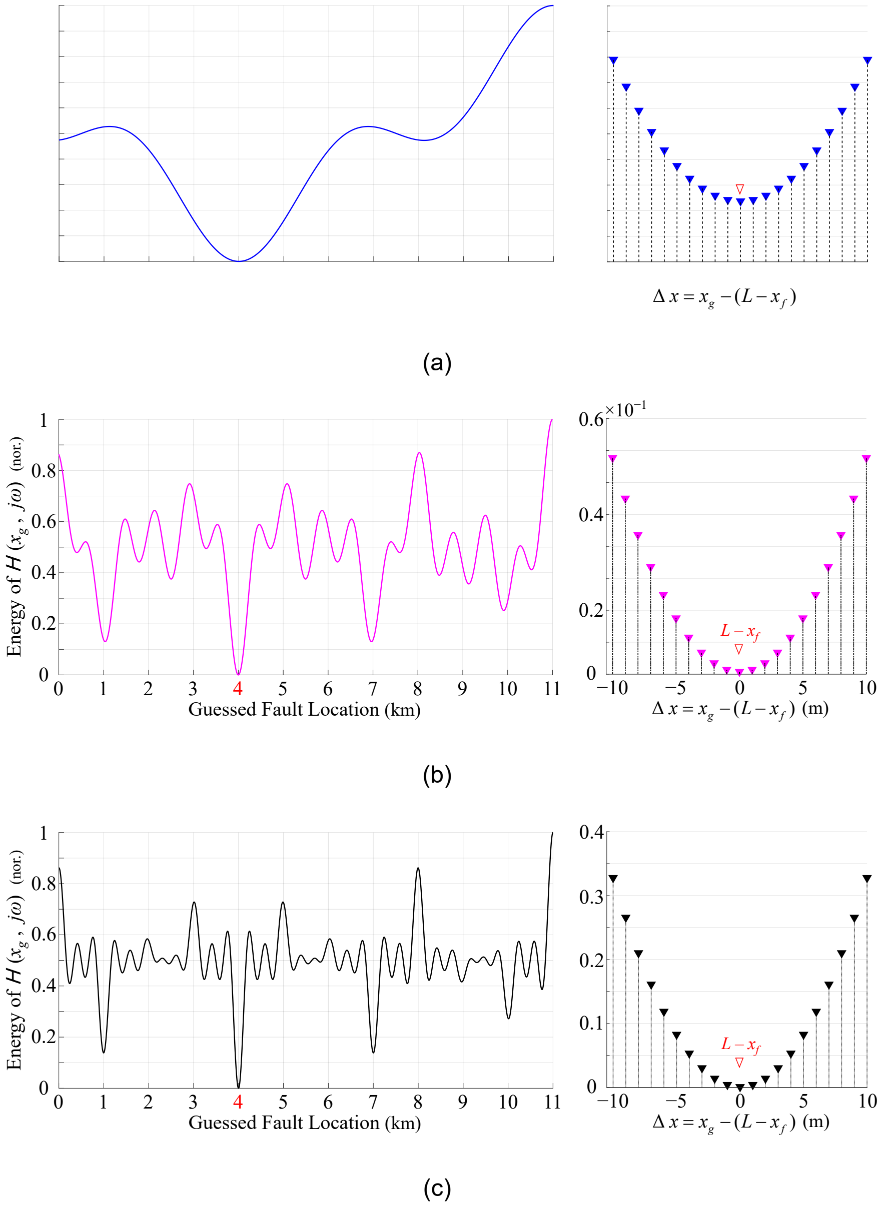

Fig. 3.10 Normalized energy of $H(x_g, j\omega)$ calculated at $\mathbb{F}^{\mathrm{DT}}$ for: (a) $N = 2$, (b) $N = 10$, and (c) $N = 20$. The fault location is assumed to be $x_f = 7$ km. In the subgraphs on the left, the guessed fault locations are defined *per* 5 m along the line. The subgraphs on the right refer to $\mathrm{d}x$ as 1 m in the neighboring region of $x_g = L - x_f$.

Given the present fault case, the energy of the reversed-time voltage, $E\{V^{\mathrm{RT}}|_{\mathbb{F}^{\mathrm{DT}}}\}$, is calculated and described as a function of the guessed fault location in Fig. 3.11. Corollary 2 is numerically validated in the example, observing that the minimum energy is located at the mirror image point $x_g = L - x_f = 4$ km. According to Fig. 3.11b, it allows identifying the mirror-image point with a better-than-1-m accuracy.

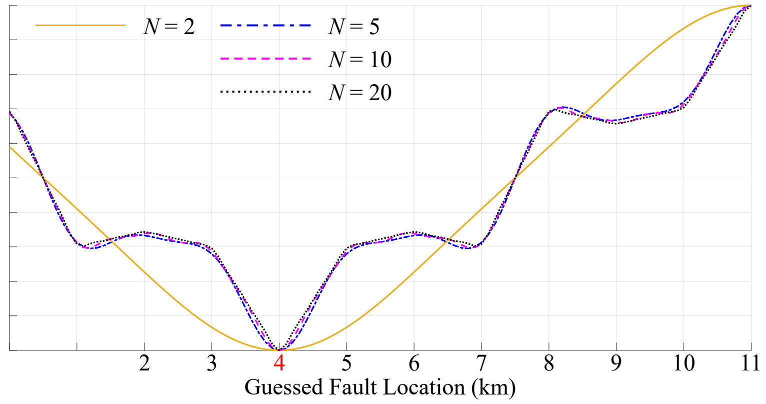

(a)

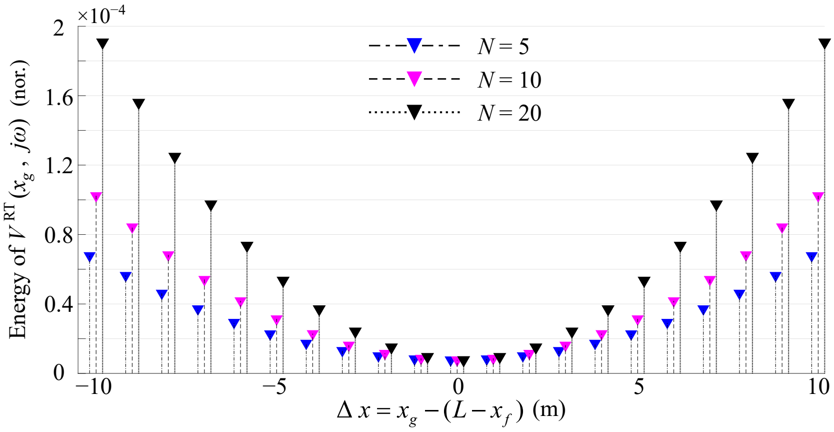

(b)

Fig. 3.11 Normalized energy of $V^{\mathrm{RT}}(x_g, j\omega)$ calculated at $\mathbb{F}^{\mathrm{DT}}$. The guessed fault locations are defined: (a) every 5 m along the line and (b) every 1 m in the spacing between $(L - x_f) \pm 10$ m.

3.2.4 Experimental Validation

This section presents an experimental validation of the property formulated in Corollary 2 by means of a reduced-scale coaxial-cable set-up.

The experiment made use of a 477-m-long standard RG-58 cable composed of two sections being 73 m and 404 m in length respectively. At the two ends of the set-up, the inner and shielding conductors of the cable were connected to lumped resistors with relatively high resistances, namely $Z_0 = 560\ \Omega$ and $Z_L = 1$ kΩ, in comparison with the 50-Ω characteristic impedance of the RG-58 cable. In this way, we considered asymmetrical reflective boundary conditions. A DC voltage of 6 V supplied the cable set-up from the line end at $x = 0$, which also served as the single observation point.

In order to emulate a real fault, a short circuit was artificially triggered between the inner and shielding conductors of the cable. The fault location was the junction of the two cable sections, namely $x_f = 73$ m. Note that the fault-initiated traveling waves propagate along the cable at speed of about 65.9 % of the speed of light and are reflected at the cable ends terminated on high resistances as well as at the junction with the presence of the short circuit. Considering that the fault location was tens of meters away from the observation point situated at the cable end $x = 0$, the resultant one-way propagation delay was in the order of hundreds of nanoseconds. That is to say, for correctly emulating the fault in such a reduced-scale cable set-up, the hardware fault emulator needs to feature a high-speed switch, which is capable of changing its status in a few nanoseconds. To address this constraint, we adopted a metal-oxide-semiconductor field-effect transistor (MOSFET) with a turn-on time of 3 ns. In the experiment, the MOSFET was driven by a NI digital input/output (I/O) card C/series 9402 that is able to generate a gate signal to the MOSFET with a sub-nanosecond rise time. It should note that the emulated fault referred to the solid-type fault since no resistor was set between the MOSFET drain and the cable inner conductor.

Figure 3.12 presents the profile of the voltage energy as a function of the guessed fault location. The normalization is implemented with respect to the maximum energy. As discussed earlier, the voltage energy was calculated in the frequency domain by summating the overall squared moduli of the components distributed in the frequency range between 1 kHz and 50 MHz. Among the guessed fault locations, which are separated from each other by 1m, the location with the coordinate $x = 404$ m is characterized by the minimum energy. The location exactly behaves as the mirror image point at $x = L - x_f$ corresponding to the emulated fault at $x_f = 73$ m with $L = 477$ m.

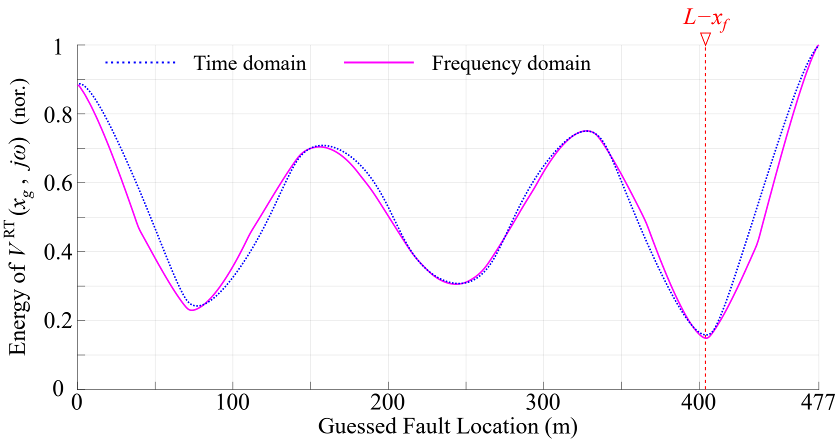

Fig. 3.12 Normalized energy of $V^{\mathrm{RT}}(x_g, j\omega)$ as a function of the guessed fault location.

Using Parseval's theorem, we also calculated the voltage energy in the time domain without the attention to identifying the switching frequency f^0 in the frequency domain. As illustrated by the blue dotted line superimposed in Fig. 3.12, the time-domain calculation produces a similar performance in terms of distributing the voltage energies at the guessed fault locations along the cable. The minimum energy again appears at the mirror image point $x = 404$ m.

3.2.5 Application Example

Although the mirrored minimum energy property is formulated using a single-phase line setup, its applicability is extended to transmission-line networks featuring multi-conductors. In what follows, we present a numerical simulation case study based on an EMTP-RV built-in 230-kV AC single circuit with a total length of 9 km. The power transformers connected to the line ends are modeled with their high-frequency input impedance of 10 kΩ. The network terminal with the longitudinal coordinate x = 0 constitutes the single observation point.

In Fig. 3.13 a to c, we present the distribution of the computed three-phase voltage energy as a function of the guessed fault location in three cases:

i) single-phase-to-ground fault at x = 2.4 km along phase *b*, i.e., *b-g* fault [see Fig. 3.13 a] ;

ii) three-phase-to-ground fault at x = 5 km, i.e., *3ph-g* fault [see Fig. 3.13 b] ;

iii) phase-to-phae-to-ground fault at x = 8.5 km along phase *a* and *c*, i.e., *a-c-g* fault [see Fig. 3.13 c].

As it can be observed in the enlarged view plotted in the respective inset figure, the minimum of the voltage energy shows in Fig. 3.13 (a) at x = 6.6 km corresponding to the *b-g* fault at x = 2.4 km, (b) x = 3 km to the *3ph-g* fault at x = 5 km and (c) x = 0.5 km to the *a-c-g* fault at x = 8.5 km. What is more, in the neighboring region of the true fault location, the distance increment is reduced to 100 m. That is to say, a better-than-100-m location accuracy is achievable by making use of the proposed mirrored minimum energy property. It is also worth underlining that the proposed property allows identifying the faulty phase(s) in addition to locating the fault. For instance, in Fig. 3.13 (a), the voltage energy at each of the guessed fault locations along the faulty phase *b* is smaller than that of its counterpart at the other two non-faulty phases.

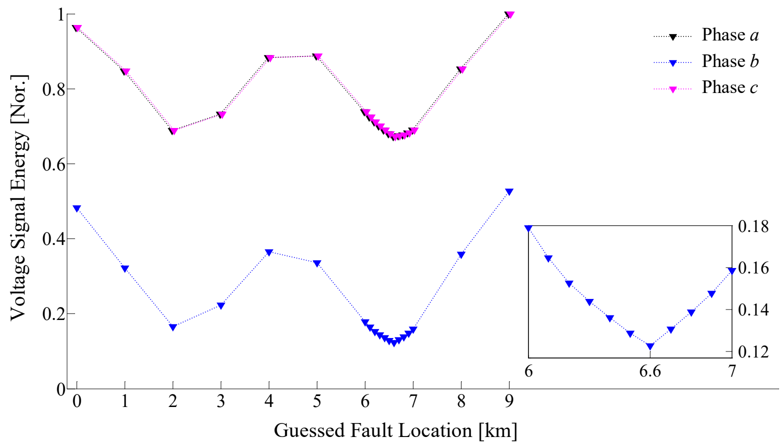

(a)

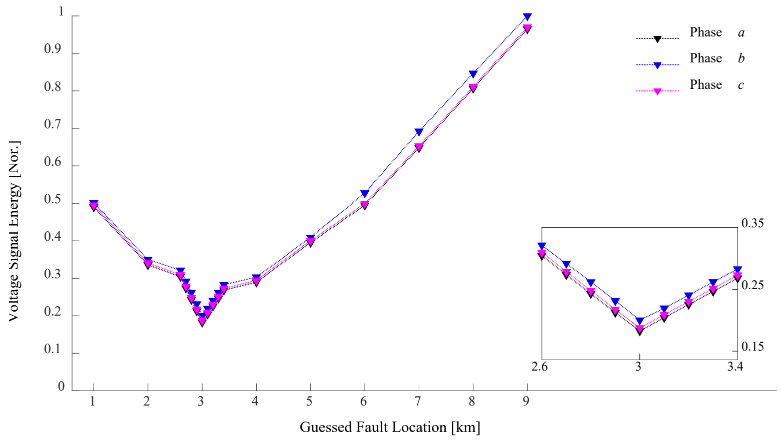

(b)

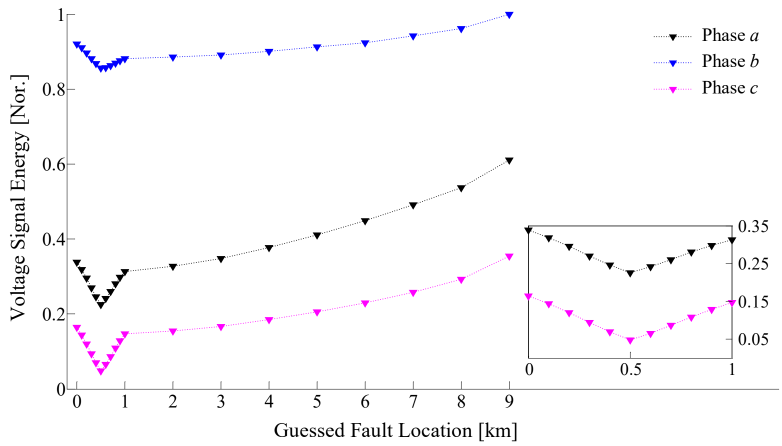

(c)

Fig. 3.13 Voltage energy as a function of the guessed fault location defined on the three phases for: (a) single-phase-to-ground fault at x = 2.4 km along phase b, (b) three-phase-to-ground fault at x = 5 km and phase-to-phae-to-ground fault at x = 8.5 km.

3.3 EMTR-based Similarity Properties and Cross-correlation Metric

The above-mentioned properties of EMTR in mismatched media currently apply to single-phase transmission lines. The ongoing study devotes attention to extending the scope towards multi-conductor topologically-complex networks. On the other hand, an EMTR-based similarity property has been proved to fulfill the motivation of enhancing the computational efficiency of the classical EMTR metrics. Moreover, a novel metric is developed to quantitatively represent the time-domain similarity. Its fault location performance has been comprehensively evaluated through simulation case studies as well as pilot tests in real power grids.

3.3.1 EMTR-based Similarity Properties

Theorem 3:

The fault current signal simulated in the reversed time (RT: fault location stage) at the true fault location $x = x_f$, denoted by $I_{x_f}^{\mathrm{RT}}(t)$, is a quasi time-delayed and scaled copy of the back-injected transient current signal, denoted by $I_0^{\mathrm{TR}}(t)$.

$I_0^{\mathrm{TR}}(t)$ is the time-reversed copy of the transients $I_0^{\mathrm{DT}}(t)$, which is measured as a response of faults in the direct time (DT: fault occurrence stage) [19],[20].

Proof

By virtue of the general boundary conditions of power networks with respect to the frequency spectrum of fault transients [21], where ρ_0^v can be approximated to +1, the following theorem is proposed.

Theorem 4:

Provided that $\rho_0^v = +1$, the local maxima of $\left|V_0^{\mathrm{DT}}(j\omega)\right|$ coincide with the Fourier expansion coefficients of a periodic square wave with a period being quadruple of the fault time delay Γ_{x_f}, which is the line one-way time delay caused by traveling-wave propagation from the fault location (i.e., $x = x_f$) to the observation point (i.e., $x = 0$) and vice versa.

The magnitude of $V_0^{\mathrm{DT}}(j\omega)$ reads

$$\left|V_0^{\mathrm{DT}}(j\omega)\right| = \frac{(1+\rho_0^v)}{\omega\sqrt{1+(\rho_0^v)^2 + 2\rho_0^v \cdot \cos[2\beta(j\omega)\cdot x_f]}} \tag{3.4}$$

The local minima of $\left|V_0^{\mathrm{DT}}(j\omega)\right|$ appear at $\mathbb{F}^{\mathrm{DT}}$ and read

$$\left|V_0^{\mathrm{DT}}(j\omega)\right|_{\omega=2\pi\cdot\mathbb{F}^{\mathrm{DT}}} = \left|H^{\mathrm{DT}}(j\omega)\right|_{\omega=2\pi\cdot\mathbb{F}^{\mathrm{DT}}} \cdot \frac{4\Gamma_{x_f}}{(2i-1)\cdot 2\pi} = \frac{\xi}{n\cdot 2\pi}, \quad i = 1,\ 2,\ 3,\ \ldots, \text{ and } n = 1,\ 3,\ 5,\ \ldots \tag{3.5}$$

where ξ is a defined magnitude coefficient.

Considering the Fourier series representation of a periodic square wave with an amplitude *A* and a duty cycle *D* as 1/2, its complex-exponential expansion coefficients are

$$\left|c_n\right| = A \cdot D \cdot \left|\frac{\sin(n \cdot \pi \cdot D)}{n \cdot \pi \cdot D}\right| = \frac{A}{n \cdot \pi}, \; n = 1, \; 3, \; 5, \; \ldots \tag{3.6}$$

Thus, the local maxima of $\left|V_0^{\mathrm{DT}}(j\omega)\right|$ fit the pattern of c_n at $\mathbb{F}^{\mathrm{DT}}$.

In the fault location stage, $V_0^{\mathrm{DT}}(j\omega)$ is time reversed and back injected by its ts Norton equivalent

$$I_0^{\mathrm{TR}}(j\omega) = V_0^{\mathrm{TR}}(j\omega) \big/ Z_0 \tag{3.7}$$

At the set of *a priori* locations $x_{\mathbb{G}}$, the fault currents are calculated as

$$I_{x_{\mathbb{G}}}^{\mathrm{RT}}(j\omega) = (1-\rho_0^v) \cdot \frac{e^{-\beta(j\omega)\cdot x_{\mathbb{G}}}}{1+\rho_0^v \cdot e^{-\beta(j\omega)\cdot 2x_{\mathbb{G}}}} \cdot I_0^{\mathrm{TR}}(j\omega) \tag{3.8}$$

From the above, $\left|I_0^{\mathrm{TR}}(j\omega)\right|$ and $\left|I_{x_f}^{\mathrm{RT}}(j\omega)\right|$ reach their respective local maxima at

$$\mathbb{F}^{\mathrm{DT}} = \mathbb{F}_{x_f}^{\mathrm{RT}} \tag{3.9}$$

with their magnitudes given by

$$\left|I_0^{\mathrm{TR}}(j\omega)\right|_{\omega=2\pi\cdot\mathbb{F}^{\mathrm{DT}}} = \frac{\xi}{n\cdot\pi} \cdot \frac{1}{Z_0} \tag{3.10}$$

and

$$\left|I_{x_f}^{\mathrm{RT}}(j\omega)\right|_{\omega=2\pi\cdot\mathbb{F}^{\mathrm{DT}}} = \frac{\xi}{n\cdot\pi} \cdot \frac{1}{Z_0} \cdot \frac{Z_0}{Z_C} = \frac{\xi}{n\cdot\pi} \cdot \frac{1}{Z_C} \tag{3.11}$$

with n being 1, 3, 5, ...

To sum up, the frequency-domain analysis indicates that the magnitude-frequency characteristics of the back-injected current $I_0^{\mathrm{TR}}(j\omega)$ and the fault current $I_{x_f}^{\mathrm{RT}}(j\omega)$ equally fit the pattern of the Fourier series coefficients of a periodic square wave with a period of $4\,\Gamma_{x_f}$. Whereas at non-fault locations, as a result of the discrepancies between $\mathbb{F}^{\mathrm{DT}}$ and $\mathbb{F}_{x_{\mathbb{G}}}^{\mathrm{RT}}$, the current waveforms are no longer square wave-like.

In the time domain, the fault-originated transient voltage observed at $x = 0$ can be analytically calculated as

$$V_0^{\mathrm{DT}}(t) = \bar{V} \cdot \varepsilon(t) + \sum_{i=1}^{m} \left\{ (1+\rho_0^v) \cdot (\rho_0^v \cdot \rho_{x_f}^v) \cdot (-\bar{V}) \cdot \varepsilon[t - t_f - (2i-1)\cdot\Gamma_{x_f}] \right\}, \quad m = 1, \; 2, \; \ldots, \; k, \; \ldots, \; M, \; \ldots \tag{3.12}$$

The first term in (3.12), namely, the product of the supplied voltage $\bar{V}$ and the unit-step function $\varepsilon(t)$ indicates that the line system has been in steady-state before the fault occurring instant t_f. The summation term quantifies the fact that the fault-originated transient response consists of multiple reflections. The upper limit m in the sum operation determines a long enough time length so that the oscillations of $V_0^{\mathrm{DT}}(t)$ sufficiently decay to 0.

Note that the time-domain time-reversal operation postulates that the considered signal is of a certain duration. To this end, a time-window function $W(t)$ is applied to truncate $V_0^{\mathrm{DT}}(t)$:

$$\tilde{V}_0^{\mathrm{DT}}(t) = \left[V_0^{\mathrm{DT}}(t) \cdot W(t)\Big|_{t_f+\Gamma_{x_f}+T_w^{\mathrm{DT}}}^{t_f+\Gamma_{x_f}} \right]\Bigg|_{t=t+t_f+\Gamma_{x_f}} \tag{3.13}$$

where the starting instant t_1 of $W(t)$ is assigned to $t_f + \Gamma_{x_f}$ so that the steady-state component of $V_0^{\mathrm{DT}}(t)$ is filtered out. In regard to the time-window length T_w^{DT}, we set it at an integral multiple of the time delay Γ_{x_f}, namely

$$T_w^{\mathrm{DT}} = M \cdot 2\Gamma_{x_f} \tag{3.14}$$

where M is large enough, ensuring that the whole transient process is covered.

It is worth mentioning that the above operation is not at the cost of losing generality. It is equivalent to extracting the fault-originated high-frequency transients. Identities (3.13) and (3.14) allow concisely formulating the fault-originated transients $\tilde{V}_0^{\mathrm{DT}}(t)$ using an analytical expression:

$$\tilde{V}_0^{\mathrm{DT}}(t) = \bar{V} \cdot W(t)\Big|_{M\cdot 2\Gamma_{x_f}}^{0} + \sum_{i=1}^{M} \left\{ (1+\rho_0^v) \cdot (\rho_0^v \cdot \rho_{x_f}^v)^{i-1} \cdot (-\bar{V}) \cdot W(t)\Big|_{M\cdot 2\Gamma_{x_f}}^{(i-1)\cdot 2\Gamma_{x_f}} \right\} \tag{3.15}$$

In the fault location stage, the direct-time observed transients $\tilde{V}_0^{\mathrm{DT}}(t)$ is reversed in time and its Norton equivalent $I_0^{\mathrm{TR}}(t)$ is determined:

$$V_0^{\mathrm{TR}}(t) = \tilde{V}_0^{\mathrm{DT}}(t)\Big|_{t=-t+T_w^{\mathrm{DT}}}, \quad I_0^{\mathrm{TR}}(t) = V_0^{\mathrm{TR}}(t) / Z_0 \tag{3.16}$$

At the guessed fault locations $x_{\mathbb{G}}$, the fault currents $I_{x_{\mathbb{G}}}^{\mathrm{RT}}(j\omega)$ can be calculated as follows

$$I_{x_{\mathrm{G}}}^{\mathrm{RT}}(t) = \frac{Z_0}{Z_0 + Z_C} \cdot \sum_{j=1}^{n} \left\{ (1+\rho_{x_{\mathrm{G}}}^i) \cdot (\rho_0^i \cdot \rho_{x_{\mathrm{G}}}^i)^{i-1} \cdot I_0^{\mathrm{TR}}(t) \cdot W(t)\Big|_{M\cdot 2\Gamma_{x_f}}^{(i-1)\cdot 2\Gamma_{x_f}} \right\} \tag{3.17}$$

In order to compensate for the quantitative difference in amplitude, $I_0^{\mathrm{TR}}(t)$ and $I_{x_f}^{\mathrm{RT}}(t)$ are normalized and with reference to their respective maximum amplitudes:

$$nor\left[I_0^{\mathrm{TR}}(t)\right] \square\, I_0^{\mathrm{TR},nor}(t) = \frac{I_0^{\mathrm{TR}}(t)}{max\left[I_0^{\mathrm{TR}}(t)\right]} \tag{3.18}$$

and

$$nor\left[I_{x_f}^{\mathrm{RT}}(t)\right] \square\, I_{x_f}^{\mathrm{RT},nor}(t) = \frac{I_{x_f}^{\mathrm{RT}}(t)}{max\left[I_{x_f}^{\mathrm{RT}}(t)\right]} \tag{3.19}$$

Let us now consider the arbitrary k^{th} edge components of $I_0^{\mathrm{TR},nor}(t)$ and $I_{x_f}^{\mathrm{RT},nor}(t)$, which read

$$nor\left(I_0^{\mathrm{TR},k}\right) = nor\left[I_0^{\mathrm{TR}}(t)\right]\Big|_{t=t_0^{\mathrm{TR},k}} \tag{3.20}$$

and

$$nor\left(I_{x_f}^{\mathrm{RT},k}\right) = nor\left[I_{x_f}^{\mathrm{RT}}(t)\right]\Big|_{t=t_{x_f}^{\mathrm{RT},k}} \tag{3.21}$$

The time lag between the sampling instants stays constant:

$$\Delta t = t_{x_f}^{\mathrm{RT},k} - t_0^{\mathrm{TR},k} = (2k-1)\cdot\Gamma_{x_f} - (k-1)\cdot 2\Gamma_{x_f} = \Gamma_{x_f} \tag{3.22}$$

the ratio of the two referring amplitudes can be calculated as

$$\eta(k) = \frac{nor\left(I_0^{\mathrm{TR},k}\right)}{nor\left(I_{x_f}^{\mathrm{RT},k}\right)} = \frac{1-(\rho_0^v)^{2k}}{1-(\rho_0^v)^{2M}} \tag{3.33}$$

Given ρ_0^v being +0.99, $\eta(k)$ the ratio approximates to +1 except for the initial small percentage of samples, which have relatively insignificant amplitudes. That is to say, most components of the two waveforms, with a time lag of Γ_{x_f} , have very similar amplitudes.

To sum up, $I_{x_f}^{\mathrm{RT},nor}(t)$ is proved to be a quasi-time-delayed copy of $I_0^{\mathrm{TR},nor}(t)$.

3.3.2 Cross-correlation Metric

The time-domain similarity between $I_0^{\mathrm{TR}}(t)$ and $I_{x_f}^{\mathrm{RT}}(t)$ is proposed to be quantitatively represented by calculating the metric of the maximum of the cross-correlation sequence, under the denomination of MCCS, as

$$R^m(x_{\mathbb{G}},l) = Max\left\{\sum_{k=0}^{K} I_0^{\mathrm{TR}}[(k+l)\cdot\Delta t]\cdot I_{x_{\mathbb{G}}}^{\mathrm{RT}}(k\cdot\Delta t)\right\},$$
$$K = T_w^{\mathrm{DT}} \big/ \Delta t\,,\ l = 0,\ \pm1,\ \pm2,\ ...,\ \pm(K-1) \tag{3.34}$$

where, $x_{\mathbb{G}}$ represents a set of guessed fault locations.

The true fault location is thus identified by

$$x_{f,\,estimated} = \arg\big|_{x_{\mathbb{G}}}\ Max\left[R^m(x_{\mathbb{G}},l)\right] \tag{3.35}$$

The step-by-step process of calculating the MCCS metric is summarized in a pseudo-algorithm presented in Table 3.1. The time-domain similarity approach requires the knowledge of the power-network topology as well as its line/cable wave propagation parameters to numerically represent the target network in a simulation environment, which is capable of simulating the transient propagation. In addition, the true fault location being unknown, a set of guessed fault locations is *a priori* defined according to the desired accuracy.

Responding to a fault event, the fault-originated transient voltage $V_{0,ph}^{\mathrm{DT}}(t)$ (with $ph = a, b, c$ for three-phase systems) can be measured at a single observation point that is assumed to be deployed at the secondary winding of a power transformer. It is implied that the time-window length T is sufficiently long (typically, one period of power frequency or longer) to record the full transient process of $V_{0,ph}^{\mathrm{DT}}(t)$.

$\tilde{V}_{0,ph}^{\mathrm{DT}}(t)$ represents the fault-originated high-frequency transients, whose spectrum contains the main components at the frequencies of the fault switching frequency and beyond. $\tilde{V}_{0,ph}^{\mathrm{DT}}(t)$ is extracted from the original transient voltage $V_{0,ph}^{\mathrm{DT}}(t)$ by means of a high-pass (HP) filter to remove the low-frequency steady-state signal.

Then, the extracted transients $\tilde{V}_{0,ph}^{\mathrm{DT}}(t)$ are truncated by a certain time-window T_w^{DT} and time reversed as $V_{0,ph}^{\mathrm{TR}}(t)$ through (3.36). For each pre-defined guessed fault location x_g, an independent electromagnetic transients simulation is performed by back injecting $V_{0,ph}^{\mathrm{TR}}(t)$ into the network model to compute the fault current signal $I_{x_g}^{\mathrm{RT}}(t)$.

The final procedure performing the fault location estimation consists of calculating the maximum of the cross-correlation sequence metric (3.34), with the global maximum of the metric indicating the fault location [i.e., (3.35)].

Table 3.1 Pseudo-Algorithm of the EMTR Cross-correlation Metric

Input:	network topology and parameters, guessed fault locations $x_{\mathbb{G}}$
	$V_{0,ph}^{\mathrm{DT}}(t),\ t \in [0, T]$
	$\tilde{V}_{0,ph}^{\mathrm{DT}}(t),\ t \in [0, T]$
	$V_{0,ph}^{\mathrm{TR}}(t) = \tilde{V}_{0,ph}^{\mathrm{DT}}(-t + T_w^{\mathrm{DT}}),\ t \in [0, T_w^{\mathrm{DT}}]$ (3.36)
for	each *a priori* guessed fault location $x_g \in x_{\mathbb{G}}$ **do**
1:	simulate the fault current $I_{x_g}^{\mathrm{RT}}(t)$ using network model and $V_0^{\mathrm{TR}}(t)$
2:	compute the MCCS metric $R^m(x_g)$
end	
	$x_{f,estimated} = arg\vert_{x_{\mathbb{G}}} Max[R^m(x_{\mathbb{G}})]$
Output:	$x_{f,estimated}$

3.3.3 Numerical Validation

In this subsection, we validate the cross-correlation metric by implementing the algorithm of Table 3.1 to locate faults in the IEEE 34-bus test distribution feeder, which is modeled in the EMTP-RV environment, as shown in Fig. 3.14.

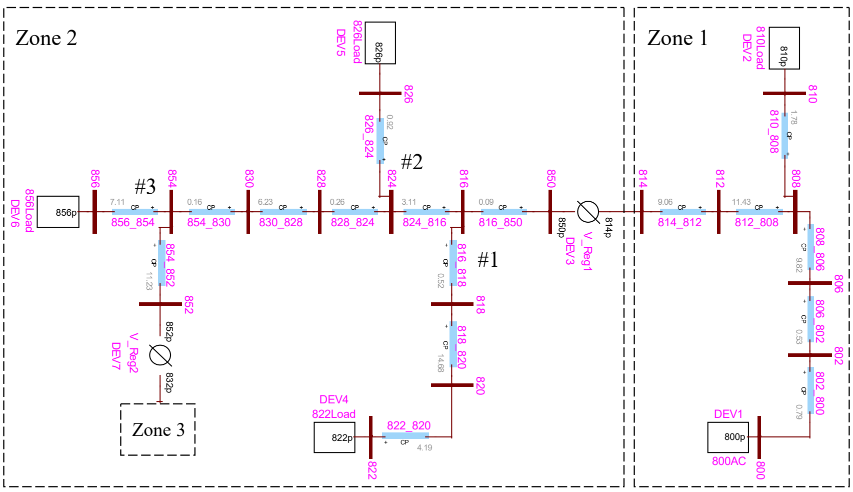

Fig. 3.14 IEEE 34-bus test distribution feeder modeled in EMTP-RV.

The case studies in this subsection consist of simulating single- and three-phase-to-ground fault (*ph*-g and 3*ph*-g) occurrences in the first zone of the feeder (between nodes 800 and 814). The second winding of the feeding transformer at node 800 is considered as the single observation point. Moreover, given that fault occurrence in power networks is a stochastic event, the fault location performance of the cross-correlation metric is evaluated with respect to the uncertainties including *i)* fault location, *ii)* fault impedance, and *iii)* fault inception angle.

As summarized in Table 3.2 the case studies consider two types of faults at each node in the tested zone, with varying values of fault impedance being 0 (solid fault), 10, 30, and 50 Ω. Additionally, the simulation is extended to near zero-crossing fault cases occurring at each of the nodes. The tested fault inception angle (θ_f) is about 4 degrees. As a result, a total of 54 fault cases are considered.

Table 3.2 Fault Cases Simulated in Zone 1 of the IEEE-34 Test Feeder

Fault type	Fault location (node)	Fault impedance (Ω)	Num. of cases
ph-g (*a*-g)	802, 804, 806, 808, 812, 814	0, 10, 30, 50	24
3*ph*-g			24
ph-g (*b*-g), $\theta_f \approx 4°$		0	6

According to the step-by-step implementation of the algorithm of Table 2.1, the time-domain similarity metric was able to accurately identify the true fault location in each tested fault case.

Figure 3.15 shows the calculated metric of the maximum of the cross-correlation sequence (MCCS) for the single-phase-to-ground fault at branch node 810. In agreement with (3.34), the MCCS metric characterizes the true fault location as well as the faulty phase (*a*) with the global maximum among the guessed fault locations. For the sake of comparison, the calculated metric for the fault, which occurs on phase *b* with a fault inception angle (θ_f) of about only 4 degrees, is superimposed in the same figure. Observe that the proposed time-domain similarity metric demonstrates a comparable performance in locating the near zero-crossing fault. As known, such faults with an extremely small fault inception angle decrease the signal-to-noise-ratio of the filtered transients and therefore degrades the performance of some traveling-wave-based fault location methods.

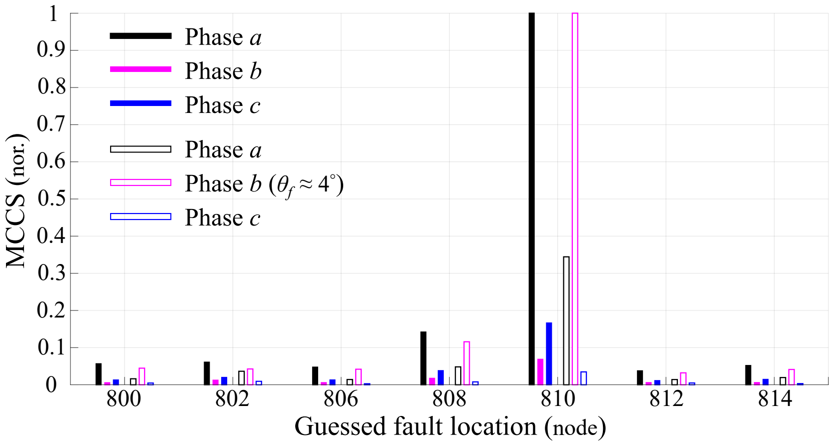

Fig. 3.15 Normalized cross-correlation metric calculated for the single-phase-to-ground fault cases at node 810. The color-filled bars represent the phase (*a*)-to-ground fault case and the white-filled bars the near zero-crossing phase (*b*)-to-ground fault case. The normalization is based on the maximum of the MCCS metric calculated for the respective fault case.

Figure 3.16 compares the calculated MCCS metric for the phase (*a*)-to-ground fault at node 812. For the sake of simplicity, only the results for the faulty phase are shown. It can be seen that the proposed cross-correlation metric is robust against the variation of the fault impedance. As discussed in [15], the EMTR reversed-time simulation does not require apriori estimation to the exact value of fault impedance. In the above-mentioned cases, the fault current is simulated by assuming a zero fault impedance [15].

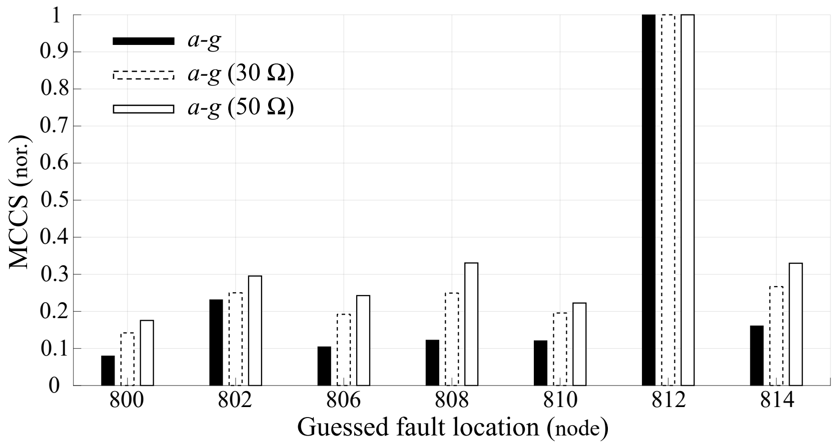

Fig. 3.16 Normalized cross-correlation metric calculated for the phase (*a*)-to-ground fault cases at node 812 with different values for the fault impedance: 0, 30, and 50 Ω. The normalization is based on the maximum of the MCCS metric obtained in the respective fault case.

Figure 3.17 presents the evaluation of the fault location performance of the MCCS metric for the three-phase-to-ground fault cases with respect to different fault locations and fault impedances. As can be seen, in spite of the uncertainties, the proposed time-domain similarity metric is still effective in locating the faults by reaching a global maximum at the respective true fault location.

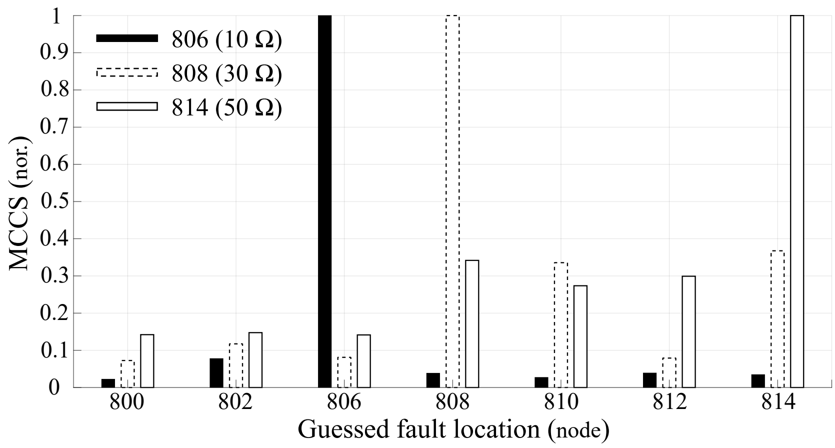

Fig. 3.17. Normalized cross-correlation metric calculated for the three-phase-to-ground fault cases: *i)* 10-Ω fault at node 806, *ii)* 30-Ω fault at node 808, and *iii)* 50-Ω fault at node 814. The normalization is based on the maximum of the MCCS metric calculated for the respective fault case.

4 Pilot Test on a Live Distribution Feeder

4.1 A prototype of the Fault Location Device

The developed EMTR-based fault location system is composed of *i)* a sensing and measurement unit, *ii)* a data acquisition block, *iii)* a triggering block, and *iv)* an embedded platform to perform the EMTR fault location process. The block diagram of the setup is shown in Fig. 4.1. The block diagram also explains the adopted hardware support for each block. With regard to the processing units, both the CPU processor and reconfigurable FPGA of the controller are used. As can be seen, the data acquisition capability is dependent on both units, while the block *iii)* and *iv)* are supported by the FPGA and the CPU of the controller respectively. The LabVIEW programming environment is used to develop the logics of the blocks *ii) - iv).*

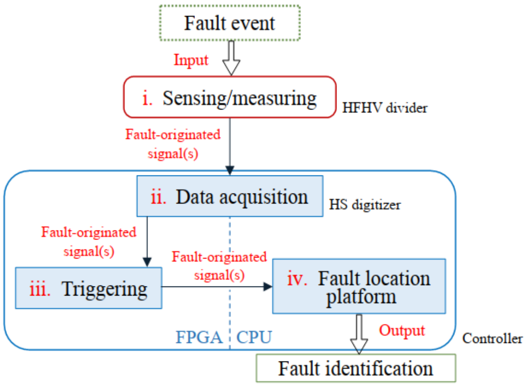

Fig. 4.1 Block diagram of the developed fault location system. The upstream processes *i) - iii)* deliver fault-originated transient signals to the platform *iv)* implementing time-reversal operation and electromagnetic transients simulations (of the EMTR backward propagation).

4.1.1 Sensing/Measuring Unit

For measuring the fault-originated electromagnetic (EM) transient signals and delivering the signals to the I/O module of the data acquisition block, the sensing/measuring devices are expected to be capable of: *i)* having sufficient bandwidth to cover the frequency spectra of the EM transient signals, and *ii)* transforming the fault signals (more than ten kV) to the withstand voltage level of the signal cables as well as the data acquisition block. Given the above considerations, a high-frequency high-voltage (HFHV) divider is used. Table 4.1 summarizes the main specifications of the adopted voltage transducer. Fig. 4.2 shows the transducer installed in a primary substation serving as the observation point) of a medium-voltage distribution network.

Table 4.1. Voltage Transducer Specifications

Rated primary voltage U_{pn}	18 kV
3-dB bandwidth	20 Hz – 4.5 MHz
Rated secondary voltage U_{sn}	1.8 V

Fig. 4.2 Medium-voltage transducer installed in the primary substation of the tested network.

It is worth mentioning that the selected sensor is able to provide zero phase error for frequencies up to 500 kHz. Therefore, post-phase correction is not needed in view of that electrical faults generally feature a frequency spectrum with the main contents up to tens of kilohertzes.

4.1.2 Data Acquisition Block

To sample the measured signals from the sensors, a NI 4-channel high-speed (HS) digitizer is utilized. This module has independent analog-to-digital converters (ADC) with a 14-bit resolution and can operate in two acquisition modes: continuous mode and record mode. In the continuous mode, the module transfers real-time data at an aggregate rate of 4 MS/s across all channels. In the record mode, the module stores samples into inboard memory at up to 20 MS/s/ch. It is also possible to combine these two modes for advanced triggering systems. This feature is exploited to develop a suitable triggering system to detect the fault occurrence (see next subsection).

4.1.3 Triggering Block

There is a need for a proper triggering system to detect the high-frequency transients resulting from the fault occurrence. Since these transients are superimposed to the network frequency (e.g., 50 Hz) component, a simple threshold-triggering criterion is generally inadequate. In this study, the triggering system is briefly described in what follows.

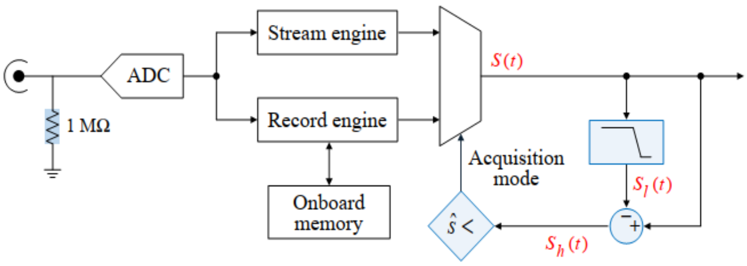

Fig. 4.3 Block diagram of the triggering block.

According to the logic structure of the triggering block shown in Fig. 4.3, first, the ADC module is operated in the continuous mode, in which it transfers in real-time the data at the rate of 1 MS/s. These data [i.e., $S(t)$ in Fig. 4.3] are used as input to a first-order Butterworth low-pass(LP) digital filter, which outputs the low-frequency components [i.e., $S_l(t)$] of the original signal. In the pilot tests, the LP cutoff frequency was set as 1 kHz. The filtered signal is subtracted from the original one, resulting in a new signal containing only the high-frequency components [i.e., $S_h(t)$] characterized by a frequency spectrum larger than the cut-off frequency. Then, when the absolute value of the obtained signal is greater than the pre-defined threshold value (i.e., $\hat{S}$), it activates the recording mode of the digitizer.

4.1.4 Fault Location Platform

The EMTR-based fault location methods are numerically implemented on a ruggedized industrial controller that uses a dual-core Intel Core processor and supports Windows Embedded Standard 7 operating system. These features allow executing third-party Windows-based simulation software on this chassis. In the performed tests, the EMTP-RV simulation environment is used to model the tested distribution network and conduct the EMT simulations in the backward-propagation stage of EMTR.

The platform processes the fault-originated transient signals delivered by the triggering block and provides fault information (e.g., fault phase and fault location) as output. First, different elements of the considered network are modeled using the network data provided by the utility. Based on the simulated network, EMTP-RV generates the corresponding simulation file containing information about network topology, components, and their parameters.

Next, the EMTR backward-propagation is simulated for every pre-defined GFL. EMTP-RV updates the original simulation file by reading the time-reversed transients and emulating the fault occurrence and runs the loop of simulating the line voltage at the GFLs.

Afterward, the generated simulation data are stored in the internal storage of the platform, and the line voltage vector of each GFL is extracted from the output data. Subsequently, the fault location metric like the energy of the voltage along the power networks is calculated and is used to identify the most likelihood fault point.

4.2 Pilot Networks

The pilot network is a radial medium voltage distribution feeder, located in the region of Fribourg, Switzerland, which connects two distribution substations. A schematic description of the network is presented in Fig. 4.4. The tested distribution feeder consists of 11.9-km long double-circuit lines (overhead lines) operating at 18/ 60 kV and multiple 18-kV three-phase laterals branching from the main feeder. The branched lines are overhead lines, underground cables, or mixed configuration, with lengths ranging from tens of meters to a few kilometers.

The medium voltage side of the primary substation (i.e., substation A in Fig. 4.4) feeding the network was selected to serve as the single observation/monitoring station and was equipped with the front-end voltage transducer together with the fault location platform described before.

Four categories of locations along the network were considered as the guessed fault locations, which include: *i)* the junctions between two overhead lines (along the main feeder), *ii)* the junctions between two underground cables, *iii)* the junctions between the main feeder and a branch lateral, and *iv)* the terminals of a branch lateral connected to load. As a result, a total of 123 guessed fault locations were a priori defined.

The numerical representation of the pilot distribution network was given in the EMTP-RV simulation environment making use of the constant-parameter (CP) line module. As to the power transformers located at the two substations (A and B) as well as at the load terminals, they were modeled considering their high-frequency input impedance of the secondary winding. To be precise, the network was grounded through a 10-kΩ resistor per phase at the above-mentioned terminals.

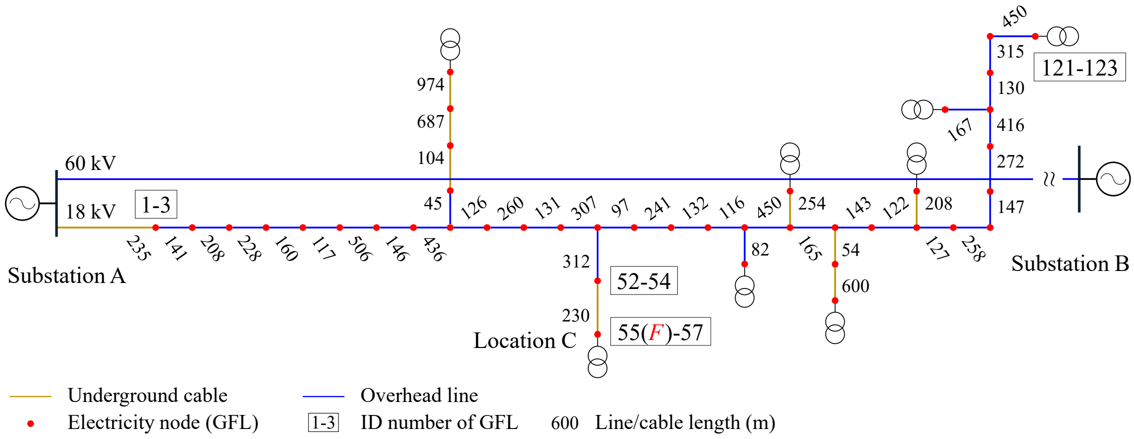

Fig. 4.4 Schematic description of the distribution network employed in the pilot test. All the electricity nodes (e.g., overhead-line towers along feeder and junctions between feeder and branch laterals) in the network are defined as guessed fault locations, which are numbered from 1 (i.e., Phase *a* at the initial terminal of the outlet cable from substation A) to 123 (i.e., Phase c at the most distant load terminal).

4.3 Fault Cases

The pilot test was carried out by intentionally triggering a single-phase-to-ground fault along one of the network laterals, as this is the most common fault type in distribution networks. Besides, as known, fault impedance can vary in a wide range and may introduce significant errors in some fault location methods. Therefore, both solid and resistive faults were emulated in the test.

Moreover, the pilot test also took account of various fault causes. In addition to permanent faults consequent upon a short circuit between a phase conductor and the ground, the test also covered transient fault events due to single and intermittent phase-to-ground arcing discharges, respectively.

In the test, the short-circuit solid fault was realized by a switching maneuver using an ABB 24-kV medium-voltage switchgear. The arcing-fault emulator was composed of a spark gap with two electrodes separated by the distances of 14 cm and 3.5 mm for the single- and intermittent-arcing faults, respectively, as shown in Fig. 4.5. In the above-mentioned fault cases, the equivalent impedance of the phase-to-ground channel/arc remained significantly smaller than the characteristic impedance of the lines/cables in the tested distribution network. The resistive fault was emulated by means of adding a 30-Ω (water) resistor into the discharge circuit of the voltage switchgear. Note that the considered impedance value is typically witnessed in resistive faults that occur in the tested distribution network.

The tested fault cases are summarized in Table 4.2 [22].

(a)

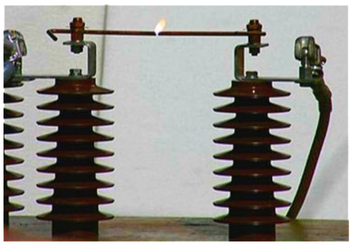

(b)

Fig. 4.5 Two types of fault emulators with spark gaps used in the pilot test. (a) A 14-cm long spark gap for the single-arcing fault and (b) a 3.5-mm long spark gap for the intermittent-arcing fault.

Table 4.2 Emulated Single-Phase-to-Ground Fault Cases in the Pilot Test

Fault type	Fault impedance	Fault cause
Solid fault	Approx.0 Ω	Short circuit
		Single-arcing discharge
		Intermittent-arcing discharge
Resistive fault	30 Ω	Short circuit

4.4 Measurement Results

As summarized in Table 4.2, two types of single-phase-to-ground faults were triggered in a specific location (i.e., Location C in Fig. 4.4) along the live network. During the pilot test, a self-developed fault location system was applied [22], successfully detecting all the emulated fault events and acquiring the fault-originated transients.

4.4.1 Solid Fault

a) Short-circuit fault

Figure 4.6 shows the voltage transient signals measured at the observation substation A when a short-circuit fault was generated in location C. The fault occurred during the positive half period of phase *a*. As it can be seen, we used a 25-ms time window, which is long enough to record the full transient process.

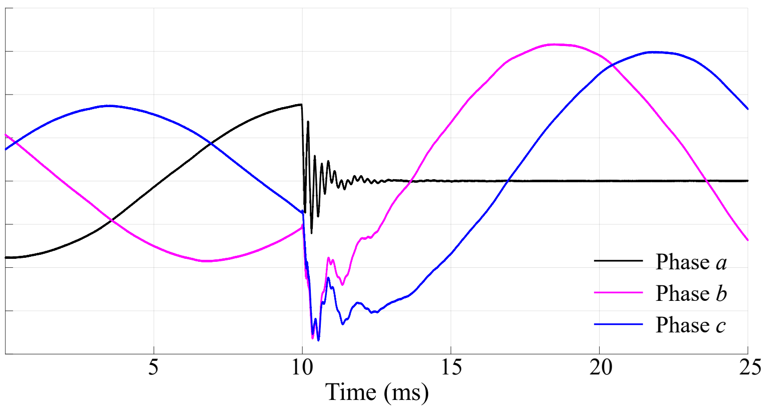

Fig. 4.6 Transient voltage signals measured in response to a solid short-circuit fault occurring in location C.

Figure 4.7 depicts the faulty phase transients within a duration of 2 ms. The transients of non-faulty phases (i.e., phases *b* and *c*) are not shown, yet the same processing was also applied to these signals.

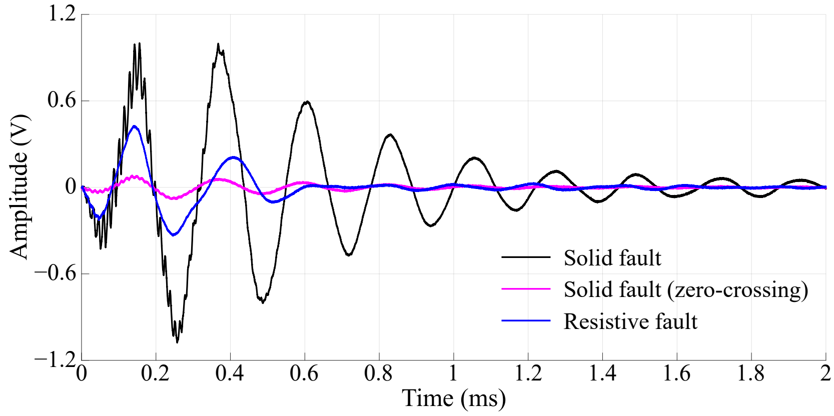

Fig. 4.7 Fault-originated transients (of faulty phase *a*) truncated to a 2-ms duration.

A similar test was especially repeated for a fault occurring near the zero-crossing instant of the phase voltage. As depicted in Fig. 4.8, the fault was generated when the faulty phase (i.e., phase *a*) voltage just crossed the zero amplitude. As known, such fault can be challenging for some triggering approaches of measuring fault-originated transients due to the difficulty in distinguishing the fault switching frequency as well as the decreased signal-to-noise ratio of the filtered transients. The filtered transients of the zero-crossing case are also shown in Fig. 4.7, showing a relatively weaker oscillation compared with those of the short-circuit fault case of Fig. 4.6. Despite this, the fault location system was able to detect the fault occurrence.

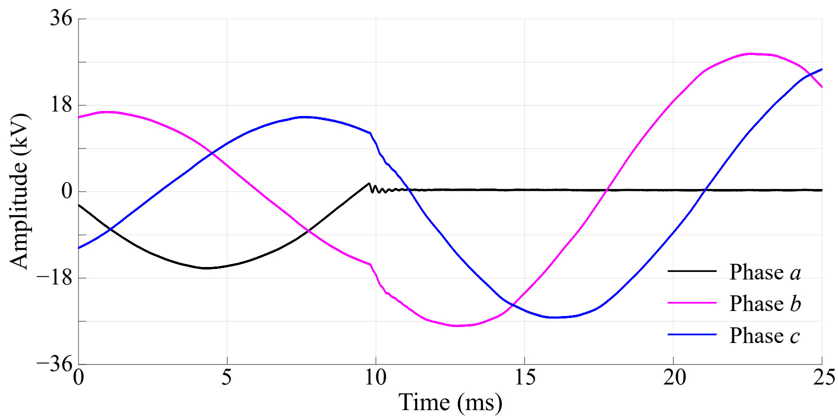

Fig. 4.8 Transient voltage signals measured in response to a zero-crossing short-circuit fault occurring in location C.

b) Single/intermittent-arcing fault

Figure 4.9 presents the voltage transient signals measured at the observation substation A for a solid type single-arcing fault case. The fault was triggered by an arc ignition between the 14-cm spaced electrodes of the spark gap during the negative half period of phase *a*. The intermittent-arcing discharge in the pilot test was specified with a double arc ignition during one 20-ms period. The inter-electrode distance of the fault emulator was reduced to 3.5 mm. The resulting faulty signals are plotted in Fig.

4.10. As can be seen, unlike the previous cases, two transient processes occur due to the first and subsequent phase-to-ground arcing discharges.

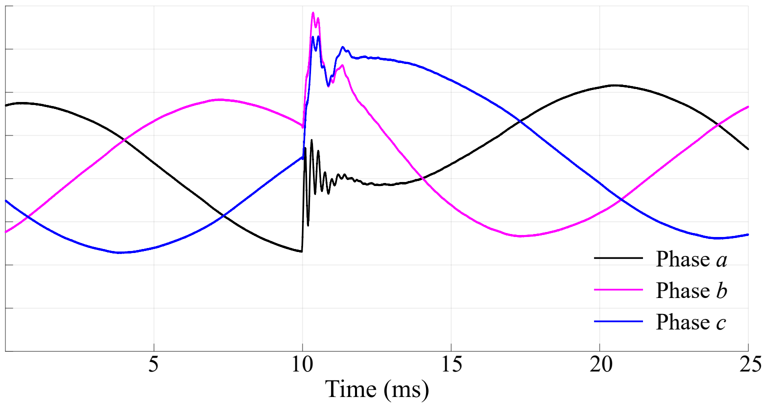

Fig. 4.9 Transient voltage signals measured in response to a single-arcing fault occurring in location C.

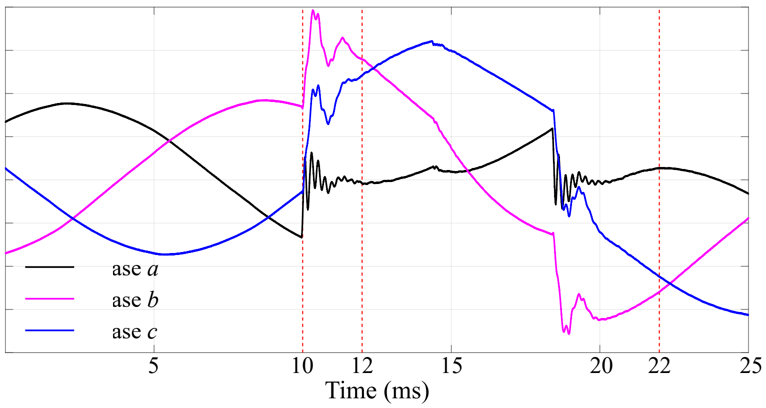

Fig. 4.10 Transient voltage signals measured in response to an intermittent-arcing fault occurring in location C.

4.4.2 Resistive fault

For the resistive fault case, a 30-Ω water resistor was connected in series with the fault emulator. The acquired fault voltage signals are depicted in Fig. 4.11. By ignoring the presence of the mutual coupling between the conductors, the faulty phase of the underground cable has a characteristic impedance of 14.6 Ω (i.e., considering the faulty phase as a single coaxial cable), thereby the voltage reflection coefficient at the fault location is positive, unlike the case of a solid fault. As can be seen in Fig. 4.7, the transients generated by the resistive fault has much faster damping compared to the solid fault case of Fig. 4.6.

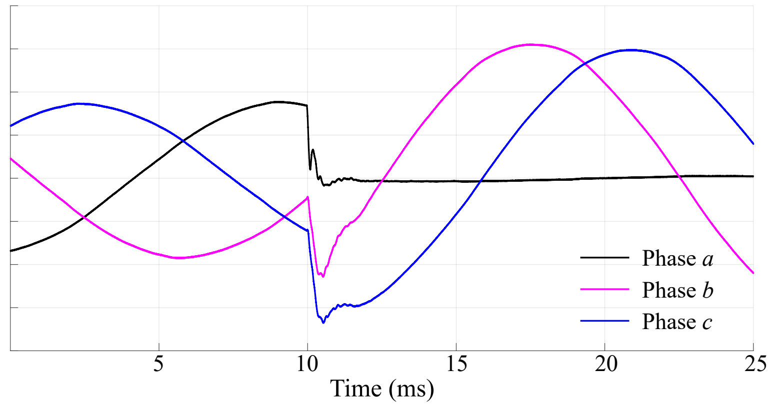

Fig. 4.11 Transient voltage signals measured in response to a resistive fault occurring in location C.

5 Performance Evaluation of EMTR-Based Cross-Correlation Metric Using Pilot Test Data

5.1 Results

The proposed EMTR similarity property based fault location approach is validated in all the fault cases. For the sake of brevity, in what follows, the fault location performance of the MCCS metric in the cases of the solid and the resistive faults are reported.

Figure 5.1 presents the calculated MCCS metric as a function of the guessed fault location for the solid fault case of Fig. 4.6. The fault was triggered during the positive-half period of Phase-*a* voltage. A total of 123 electricity nodes in the tested network were defined as the guessed fault locations. As it can be seen, the true fault location, numbered 55, is characterized as the global maximum in agreement with the criterion of (3.35).

Further validation is conducted using the acquired data of a near-zero-crossing case of Fig. 4.8, aiming at assessing the MCCS metric with respect to the fault with a relatively small inception angle. The distribution of the calculated MCCS metric as a function of the guessed fault location is illustrated in Fig. 5.2. It is evident that both the exact fault location and the faulty phase are identified. The above-discussed results (of Fig. 5.1 and Fig. 5.2) experimentally validate the robustness of the time-domain similarity property and the resultant MCCS metric against the fault inception angle.

Figure 5.3 presents the calculated values of the MCCS metric at the respective guessed fault locations for the 30-Ω phase (*a*)-to-ground fault case of Fig. 4.10. In spite of the faster-damping high-frequency transients compared to those of the solid faults, the proposed MCCS metric is still effective in evaluating the similarity between the back-injected transients and the fault current simulated at the true fault location, which is thus indicated in Fig. 5.3 as the global maximum of the MCCS metric.

The presented analysis using the pilot test data experimentally validates the EMTR similarity property and demonstrate the capability of the MCCS metric in dealing with realistic faults.

The calculated MCCS metric also shows a second peak value at the adjacent guessed fault location numbered 52. These two locations are the two ends of the 230-m long faulty underground cable (see Fig. 4.4). An analysis of achievable fault location accuracy is detailed in the following subsection.

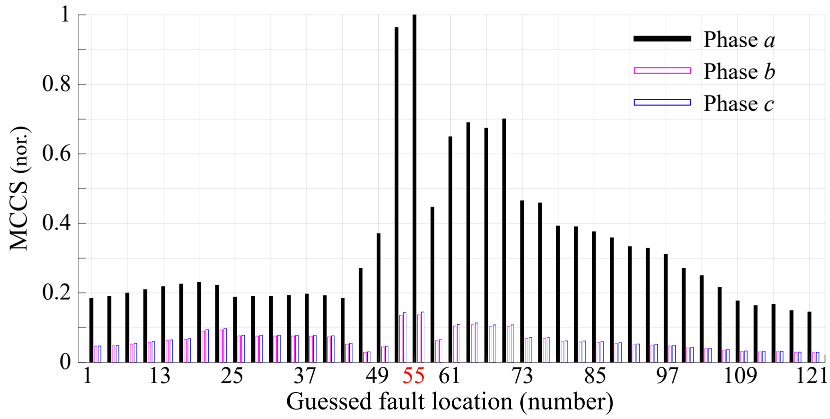

Fig. 5.1 Normalized cross-correlation metric calculated for the solid phase (*a*)-to-ground fault.

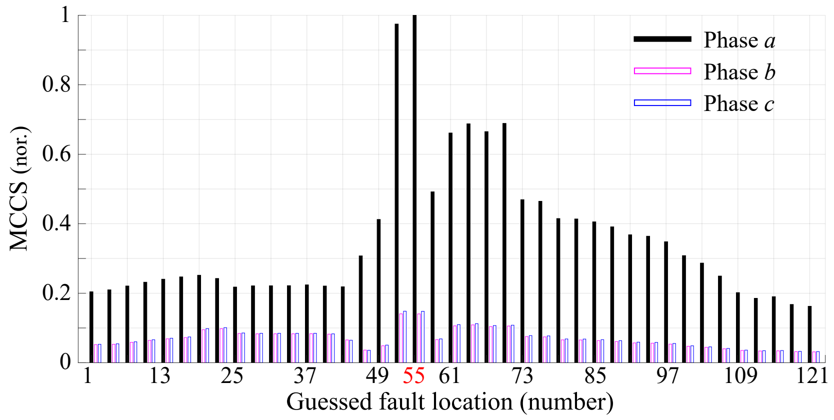

Fig. 5.2 Normalized cross-correlation metric calculated for the near zero-crossing phase (*a*)-to-ground fault.

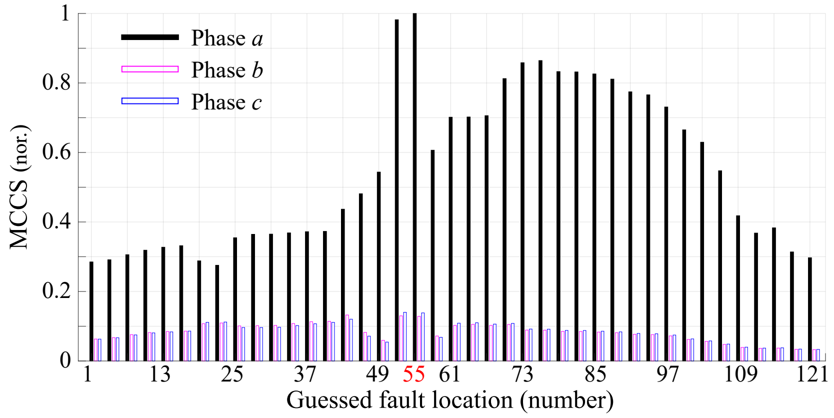

Fig. 5.3 Normalized cross-correlation metric calculated for the resistive phase (*a*)-to-ground fault.

5.2 Performance Analysis: Comparing the MCCS metric with the Classical EMTR Metric

5.2.1 Fault Location Accuracy

In practice, for the sake of minimizing the computation time, the EMTR-based fault location process can be conducted successively in two steps. In the first step, only the so-called electricity nodes (e.g., overhead-line towers along the main feeder, junctions between the main feeder and lateral branches) are considered as guessed fault locations. For the tested distribution network, a total of 123 electricity nodes are defined (see Fig. 4.4). This first step identifies, in a relatively short time, the faulty line/cable. Then, an off-line analysis further subdivides the faulty line/cable into shorter sections according to user-desired location accuracy.

The presented results show that the global maximum is reached at the true fault location (i.e., the guessed fault location numbered 55). The calculated MCCS metric also shows a second peak value at the adjacent guessed fault location numbered 52. These two locations are the two ends of the 230-m long faulty underground cable (see Fig. 4.4). The cable was subdivided into 23 sections in order to reach a location accuracy of 10 m. Accordingly, the off-line simulations were performed with a finer time step of 5 ns, which is smaller than one-tenth of the wave propagation delay of the 10-m cable section.

In Fig. 5.4a, the MCCS metric is presented as a function of the distance from the left end of the faulty cable. It is shown that the energy reaches its maximum at the true fault location (i.e., the right end of the cable) in the emulated solid fault case the resistive fault case as well. Because of the highly similar behaviors compared with that of the solid fault case, the results calculated for the cases of arcing faults are not presented. Meanwhile, for the sake of comparison, the fault location performance of the classical EMTR fault current signal energy (FCSE) metric (e.g., [15]) with respect to the two fault cases is illustrated in Fig. 5.4b.

The obtained results confirm that the true fault location (i.e., the right end of the cable) still features the maximum of the MCCS metric as well as of the FCSE metric, thus, show a better-than-10-m location accuracy for the tested fault cases.

To sum up, the proposed MCCS metric is capable of providing comparable fault location performances in terms of the fault location accuracy and the applicability of various types of realistic faults.

5.2.2 Computation Efficiency

We now discuss the advantage of the proposed cross-correlation metric based on the similarity property over the other classical EMTR fault location metrics (e.g., FCSE), with a particular emphasis on computation efficiency.

If we define the time delay between the two instants of fault detection and fault location as the response time of a fault location method, the response time of the method using the EMTR-FCSE metric is mainly determined by the time consumption of simulating the fault current signal at a single guessed fault location and the total number of the guessed fault locations.

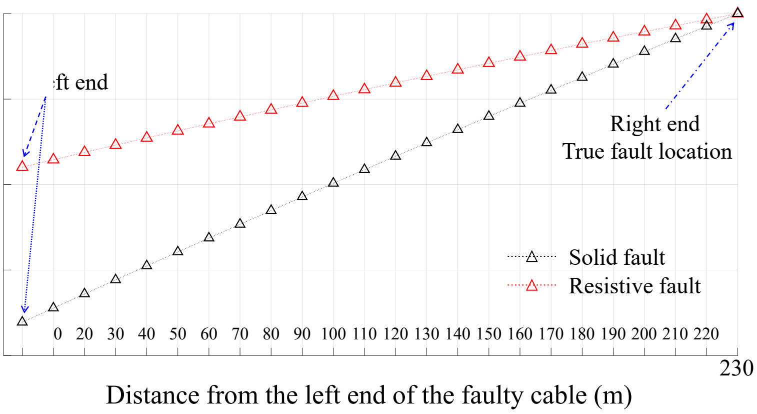

(a)

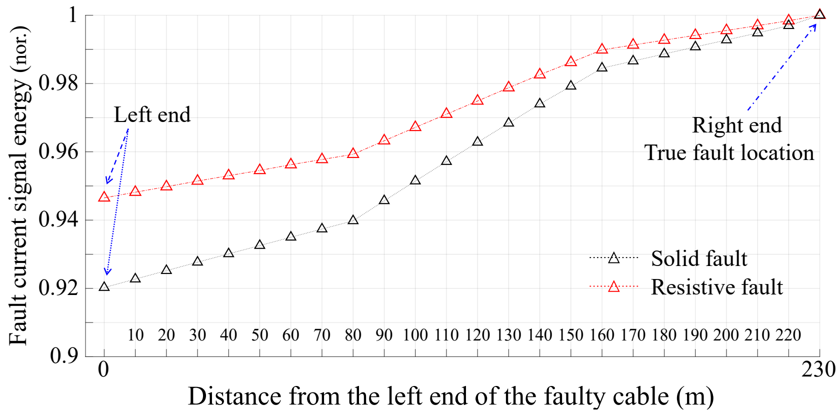

(b)

Fig. 5.4 (a) Normalized fault current signal energy metric and (b) normalized cross-correlation metric calculated as a function of the distance from the left end of the faulty cable.

As discussed, the proposed cross-correlation metric evaluates the similarity between $I_0^{\mathrm{TR}}(t)$ and $I_{x_{\mathbb{G}}}^{\mathrm{RT}}(t)$ in the time scale of the duration of the back-injected transients [e.g., T_w^{DT} of $I_0^{\mathrm{TR}}(t)$]. In other words, the MCCS metric requires simulating the fault current signals [e.g., $I_{x_{\mathbb{G}}}^{\mathrm{RT}}(t)$] only in the duration of T_w^{DT}, as opposed to the fault current signal amplitude or energy metric (e.g., [10], [15]) requiring the observation of the full waveforms of $I_{x_{\mathbb{G}}}^{\mathrm{RT}}(t)$ in the duration T_w^{RT}, which, in general, is twice as long as T_w^{DT}.

As a result, the proposed time-domain similarity approach considerably reduces the simulation time consumption *per* guessed fault location and, therefore, benefits a faster response of identifying fault occurrences.

6 Analysis of Impact of Incomplete Knowledge of Network Parameters on Fault Location Accuracy of EMTR Fault Current Signal Energy Metric

The fault location performance of traveling-wave-based techniques, including EMTR-based methods, is commonly impacted by inadequately or inaccurately modeling target power networks in simulation environments. Incomplete or outdated knowledge of transmission lines in power networks in terms of geometrical and electrical parameters is considered to be a primary cause of such degradation. Within this context, a simulation study is carried out to examine the fault location accuracy of EMTR metrics in the scenarios where per-unit-length (p.u.l) parameters of transmission lines used in the time-reversed simulations deviate from respective nominal values. To be specific, the simulation refers to typical 20/380-kV overhead lines and underground cables, whose p.u.l parameters are summarized in Table 6.1.

Table 6.1 Per-Unit-Length (P.U.L.) Parameters of 20/380-kV Overhead Lines/Underground Cables

	20-kV	380-kV
	Overhead lines	Underground cables
P.u.l. resistance (Ω/m)	0.268×10^{-3}	0.025×10^{-3}
P.u.l. inductance (H/m)	1.1×10^{-6}	0.71×10^{-6}
P.u.l. capacitance (F/m)	10.7×10^{-12}	266×10^{-12}

EMTR-based fault location metrics are dependent on analyzing the process of fault-originated traveling waves that propagate along a faulty power network (i.e., matched-media-based metrics) or a non-faulty one (i.e., mismatched-media-based metrics). Therefore, the fault location performances of those metrics are sensitive to the variation of the velocity of wave propagation. The electromagnetic transients originated by faults in power systems are generally characterized by a spectrum dominating across the frequencies that range from some kilohertz, in which the low-loss approximation in transmission-line theory is justified for typical overhead lines and underground cables. As a consequence, the velocity of propagation is, to a first approximation, determined by the parameters of p.u.l inductance (l) and capacitance (c), namely

$$v = \frac{1}{\sqrt{lc}} \tag{6.1}$$

Given the above, the simulation assesses the fault location accuracy as a function of the deviations of p.u.l inductance and capacitance from nominal values, respectively. The EMTR with the classical metric of fault current signal energy (FCSE) is used to estimate the true fault location.

a) Fault case along 20-kV overhead lines

Tables 6.2 and 6.3 report the fault location accuracy of the EMTR-FCSE in response to deviations in the line parameters ranging from $\pm1\%$ to $\pm50\%$. The guessed fault location is defined along the line with an increment of 10 m. The fault location error is calculated by

$$Fault\ location\ error\ (\%) = \frac{\left|x_f - x_{f,estimated}\right|}{L} \times 100 \tag{6.2}$$

As it can be anticipated, the fault location error tends to increase as the deviation in the line parameters (either inductance or capacitance) increases. The EMTR-FCSE metric tolerates a slight discrepancy between the nominal values and their counterparts, which are employed to model the transmission line. Precisely, a deviation of 10% or less on the line per-unit-length inductance or capacitance would result in a location error of less than 5%.

Table 6.2 Fault Location Error Caused by a Deviation in Terms of p.u.l. Inductance For the Fault Case along 20-kV Overhead Lines

	$L = 10$ km, $x_f = 8.6$ km							
Deviation from nominal p.u.l. inductance	$+1\%$	-1%	$+10\%$	-10%	$+20\%$	-20%	$+50\%$	-50%
Estimated fault location (km)	8.56	8.64	8.2	9.07	7.85	9.62	7.02	4.05
Faul ocation error (%)	0.4	0.4	4	4.7	7.5	10.2	15.8	45.5

Table 6.3 Fault Location Error Caused by a Deviation in Terms of p.u.l. Capacitance for the Fault Case along 20-kV Overhead Lines

	$L = 10$ km, $x_f = 4.25$ km							
Deviation from nominal p.u.l. capacitance	$+1\%$	-1%	$+10\%$	-10%	$+20\%$	-20%	$+50\%$	-50%
Estimated fault location (km)	4.23	4.27	4.05	4.48	3.88	4.75	3.47	6.01
Faul ocation error (%)	0.2	0.2	2	2.3	3.7	5	7.8	17.6

b) Fault case along 380-kV underground cables

Tables 6.4 and 6.5 present the fault location performance of EMTR-FCSE with respect to dealing with the fault cases along the 380-kV underground cable. As discussed previously, a higher fault location accuracy relies on the fact that the employed line parameters are reasonably consistent with the ones in the real world. It can be seen that cables are less sensitive to line parameter uncertainties compared to overhead lines, essentially because the wave propagation speed is lower.

Table 6.4 Fault Location Error Caused by a Deviation in Terms of p.u.l. Inductance For the Fault Case along 380-kV Overhead Lines

	$L = 14$ km, $x_f = 5.2$ km							
Deviation from nominal p.u.l. inductance	$+1\%$	-1%	$+10\%$	-10%	$+20\%$	-20%	$+50\%$	-50%
Estimated fault location (km)	5.17	5.22	4.96	5.48	4.74	5.81	12.73	7.35
Faul ocation error (%)	0.21	0.14	1.71	2	3.29	4.36	53.79	15.36

Table 6.3 Fault Location Error Caused by a Deviation in Terms of p.u.l. Capacitance for the Fault Case along 380-kV Overhead Lines

	$L = 14$ km, $x_f = 10.7$ km							
Deviation from nominal p.u.l. capacitance	$+1\%$	-1%	$+10\%$	-10%	$+20\%$	-20%	$+50\%$	-50%
Estimated fault location (km)	10.65	10.75	10.2	11.28	9.77	11.96	8.74	9.08
Faul ocation error (%)	0.36	0.35	3.57	4.14	6.64	9	14	11.57

As discussed in [22], by comparing simulated fault-originated transients with the measured ones, the numerical model can be optimized in terms of reaching an admissible precision of representing target power networks in the simulation environment.

7 Optimal Sensor Placement

In the time reversal technique, an optimal placement of the sensor(s) to record the voltage signals produced by the fault is key to ensure a maximum efficiency and full observability of the network. In order to perform the task of determining the optimal placement of the sensor for a given network, we have considered and implemented two different methods:

1) Decomposition of the time reversal operator (DORT)

2) Classical optimization technique

7.1 A Decomposition of the Time Reversal Operator (DORT)

The time reversal technique has been proposed by Prof. Fink and his team, first in the field of acoustics. Later, the time reversal technique was applied to the field of electromagnetics and applied to various other areas of electrical and computer engineering such as in radar, remote sensing, and imaging using either optic, acoustic or electromagnetic waves. To increase the efficiency of the method in particular in the detection of multiple objects (scatterers or targets), extensions of the time reversal technique were proposed, the most important ones being DORT (from the french Décomposition de l'Operateur de Retournement Temporal, Decomposition of Time Reversal Operator) or TR-MUSIC (MUltiple SIgnal Classification) techniques.

Prada and Fink showed that the DORT method is able to selectively focus the waves on multiple objects. It should be noted that, in the DORT method, the eigenvector(s) correspond to the objects (scatterers) and they are used in the backpropagation step to focus on the selected object(s). While, in the TR-MUSIC method, the singular values of the null space are used to locate multiple objects [6]. In other words, the basic idea behind both the DORT and MUSIC is the decomposition of the time reversal operator matrix (or the multistatic data matrix that will be defined later) into the signal and noise subspace. The DORT method uses the signal subspace while the MUSIC method uses the noise subspace.

In the present study, we have used the DORT approach to focus on the selected scattering object by using the corresponding eigenvector. In this technique, the number of transducers (transmitter and receiver) should be greater than the number of scatterers (objects) and the scatterers should be well-resolved in space. For example, consider an array of *N* transducers which transmit electromagnetic/acoustic waves to M well-resolved scatterers. It is assumed that the system is linear and time invariant. In this case, we can define a *N*×*N* interelement impulse response matrix, where h_pq (t) is the impulse response when the qth transducer transmits a delta function toward the pth receiver. The received signal r_p (t) for each transducer can be written as

$$r_p(t) = \sum_{q=1}^{N} h_{pq}(t) \otimes s_q(t) \tag{7.1}$$

where, $s_q(t)$ and $\otimes$ are the transmitted signal by transducer q and the convolution operator, respectively. The parameters *p* and *q* can be varied in the range of 1 to *N*. Equation (7.1) can be rewritten in the frequency domain using the Fourier transform as,

$$R(\omega) = H(\omega)S(\omega) \tag{7.2}$$

where R(ω) is the *N*×1 received vector, H(ω) is the *N*× *N* transfer matrix, and S(ω) is the *N*×1 transmitted vector. ω is angular frequency. It should be noted that in this report, capital letters are used to represent vectors and matrices.

In the frequency domain, the time reversal operator is equivalent to the phase conjugation. For this reason, we will conjugate the received signal in the forward step, R(ω), and back propagate it into the same media. Using the reciprocity theorem (H^t (ω)=H(ω)), the received signal at the position of the sending transducer following the back-injection of the time-reversed signal can be written as

$$R^{TR}(\omega) = H^t(\omega)R^*(\omega) = H^t(\omega)H^*(\omega)S^*(\omega) = H(\omega)H^*(\omega)S^*(\omega) \quad (7.3)$$

where, t and * denote respectively the transpose and conjugate operators. In DORT, the matrix H^* (ω)H(ω) is defined as the time reversal operator (TRO). We can easily calculate the eigenvalues λ_i (ω) and eigenvectors, V_i (ω) of the TRO, i.e., H^* (ω)H(ω).

Let us consider the transmitted signal in the forward step to be one of the eigenvectors, i.e., V_i (ω), namely the ith column of eigenvectors matrix. After the TR process, the received signals according to (7.3) is λ_i (ω) V_i^* (ω), that is proportional to the complex conjugate of the ith column of the eigenvectors matrix, λ_i (ω) being the ith eigenvalue. In other words, using the DORT method, one can focus on the selected object using the decomposition of the TRO.

7.2 Application of DORT to the Problem of Optimal Placement of the Sensor In a Power Transmission Line Network

We have implemented the DORT method to find the optimal placement of the sensor in a power transmission line network. By using the DORT method, one can determine the most prominent scatterers, namely the network junctions, in terms of the associated reflections. The most prominent scatterer in terms of its associated reflections corresponds to the largest eigenvalue. The junction (node) corresponding to the weakest reflections can be selected as the suggested position for the placement of the sensor.

In power networks, the transmission lines are commonly terminated by transformers with high impedances (10-100 kΩ), causing significant wave reflections. The main limitation of the DORT method to find the optimal placement of the sensor in power networks is that multiple reflections between the junctions in the power network might result in non-resolved junctions. In real power networks, the number of terminals (feeding transformers) is commonly less than the junctions. This means that the number of scatterers (junction points) isgreater thanthe number of transducers (terminal points). This means that the DORT method would not be always able to handle this situation. To examine the efficiency of the DORT method, we have applied it to (i) a 2D scattering problem and to (ii) a transmission line network.

7.2.1 2D Scattering Problem

In the considered 2D scattering problem, it is assumed that we have two well-resolved 2D scatterers as shown in Fig. 7.1. The distance between the two scatterers is 0.2λ, while the distance between the antennas are 0.5λ and λ, respectively.

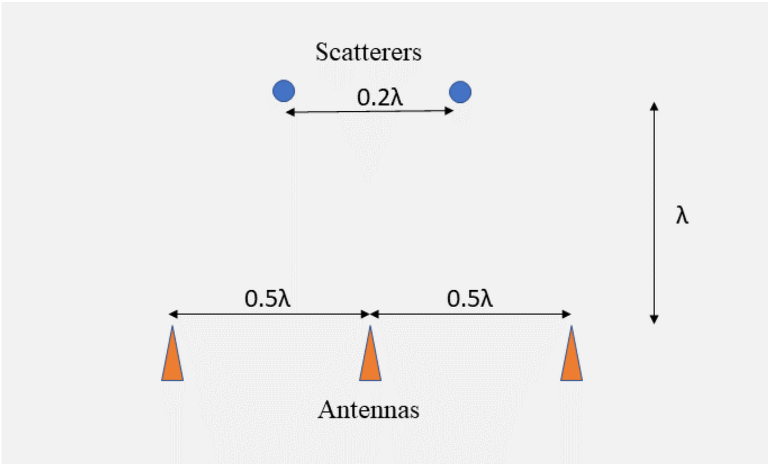

Fig. 7.1 The geometry of the problem with two scatterers and three antennas.

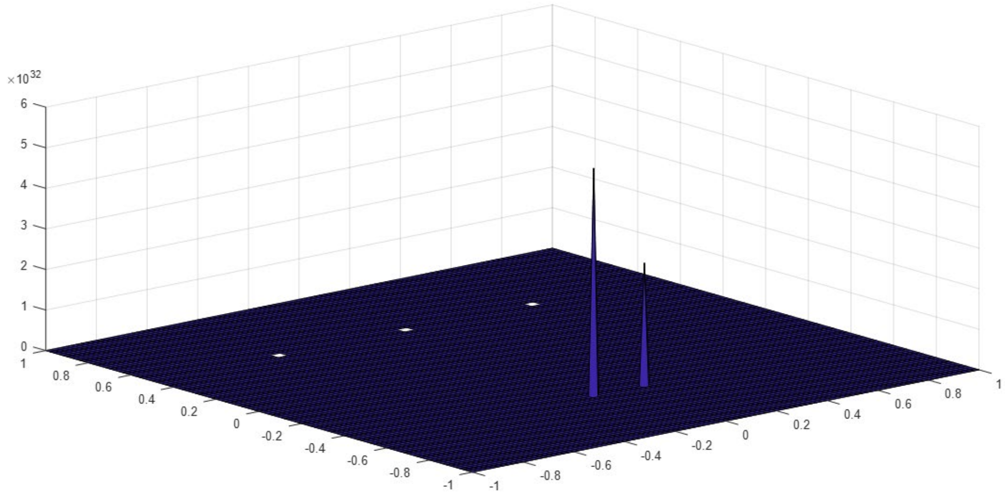

Fig. 7.2 The location of the antennas (white points) and the scatterers (sharp bars).

The results obtained applying the DORT method are depicted in Fig. 7.2. In this figure, the white points show the location of the antennas and the location of the scatterers as determined using the DORT technique are shown with vertical bars. The amplitudes of the vertical bars correspond to the respective singular values. In this example, we have two well-resolved scatterers that means we should have only two non-zero singular values. In practical cases, due to the presence of noise, all the singular values are non-zeros. To determine the number and location of scatterers, a threshold value according to the dynamic range of the measurement devices are used. This means that all the singular values lower than the minimum dynamic range of the measurement devices are considered as zero. As can be seen in this figure, the DORT method can easily determine the location of the scatterers.

Figure 7.3 shows the singular values obtained by the DORT method. As we can see in this figure, we have only two non-zero singular values that are exactly equal to the number of scatterers. As a result, when the number of scatterers is greater than the number of antennas (in transmission line networks, this means that the number of junctions is greater than the number of terminals, which is commonly the case), the DORT method cannot help us to determine the number and location of scatterers. In other words, the DORT method is not useful to determine the reflectivity from the junction to determine the location of the sensor.

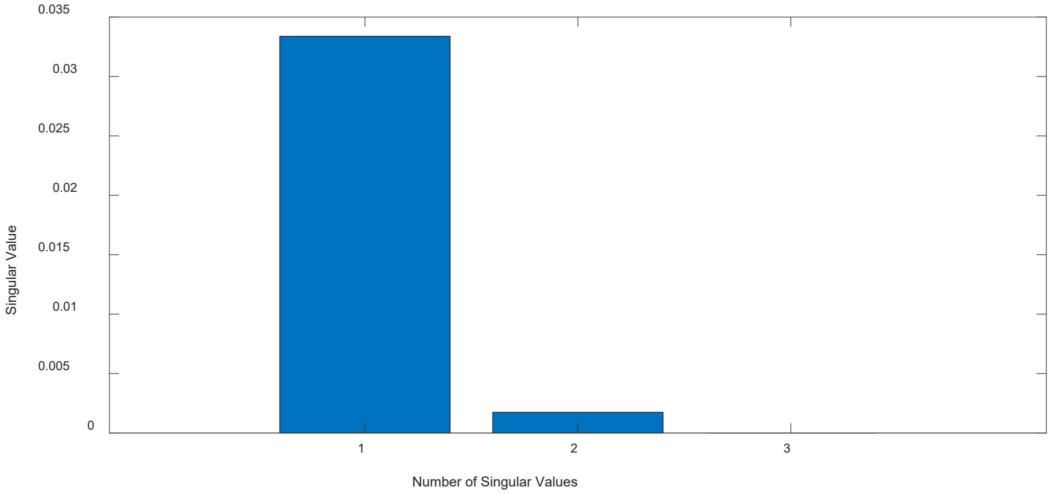

Fig. 7.3 The singular values obtained in the DORT method.

7.2.2 Transmission Line Network

We did a similar simulation for a transmission line network whose configuration is shown in Fig. 7.4. The network is composed of a main overhead transmission line between Port 1 and Port 3 as shown in Fig. 7.4. The length of this main section is 1875 m. The network also contains three lateral branches. The first branch from the left is an underground cable with a length of 208 m. The second and third branches are overhead transmission lines with lengths of 167 m and 760 m, respectively.

The singular values of the network are shown in Fig. 7.5. As can be seen in this figure, all the singular values are non-zero, meaning that the number of junctions with main reflection is greater that the number of terminals. So, the number of junctions can not be determined using the DORT technique.

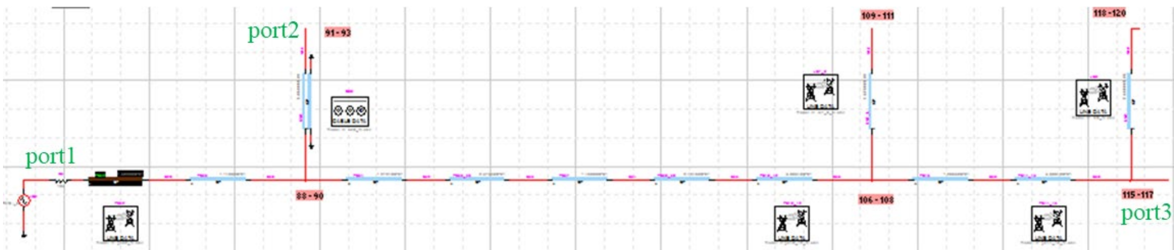

Fig. 3.4 The configuration of the assumed single-phase transmission line.

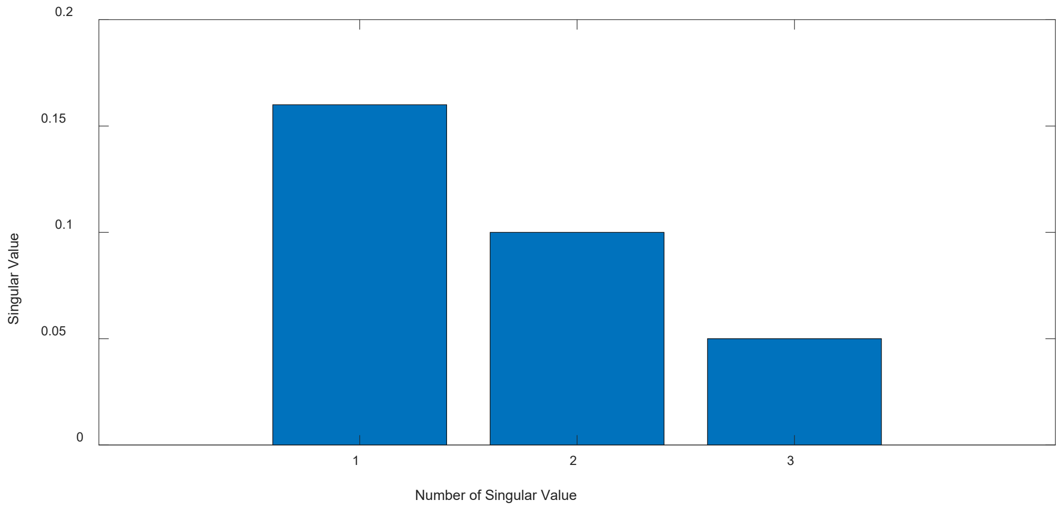

Fig. 7.5 The singular values obtained in the DORT method.

7.3 Optimization Technique

The optimal placement means solving the following optimization problem: finding the appropriate location of the sensor, at which the EMTR method is able to locate all the possible fault locations along the entire power network. It should be noted that this problem is accompanied by constraints related to the possible locations for the sensors. It can be anticipated that not all the nodes of the network could accommodate in the same manner the installation of the sensor, either because of economic considerations or installation challenges.

All the optimization techniques attempt to minimize or maximize an objective function. To do this, the optimization techniques use a procedure, sometimes iterative, to compare the various solutions to obtain an optimum or a satisfactory solution. Nowadays, the presence of high-speed computers has led optimization techniques to become part of scientific and engineering activities. Optimization techniques can be classified into many categories, some of them are briefly described in what follows.

Deterministic versus heuristic algorithms: In the deterministic algorithms, specific deterministic rules are used to find the optimum result. When deterministic approaches to find an optimal solution are impractical, heuristic approaches can be used to find a satisfactory solution, even though the solution cannot be guaranteed to be optimal.

Continuous optimization versus discrete optimization: In the continuous optimization, the objective function is only composed of continuous variables while in the discrete optimization techniques, the variables of the objective function are discrete. There is another type of optimization technique where the variables of the objective function are mixed, namely some are discrete and some continuous. This latter is referred to as mixed discrete and continuous optimization problem.

Constrained optimization versus unconstrained optimization: In constrained optimizations techniques there are at least one constraint for at least one of the variables in the objective function. The optimization technique without any constraints are called unconstrained optimization problem.

Single or multiple objective optimization techniques: In the objective optimization, we have only one objective function that should be optimized while in multiple objective problems, there are more than one objective function to optimize.

In the case of distribution power networks, possible locations to install the sensor is limited and, in most cases, they do not exceed 10. In this case, there is no need to apply a sophisticated optimization technique. However, in cases when the number of possible nodes to install the sensor are significant and/or the number of possible fault locations is large, heuristic approaches such as genetic algorithm (GA) can be applied.

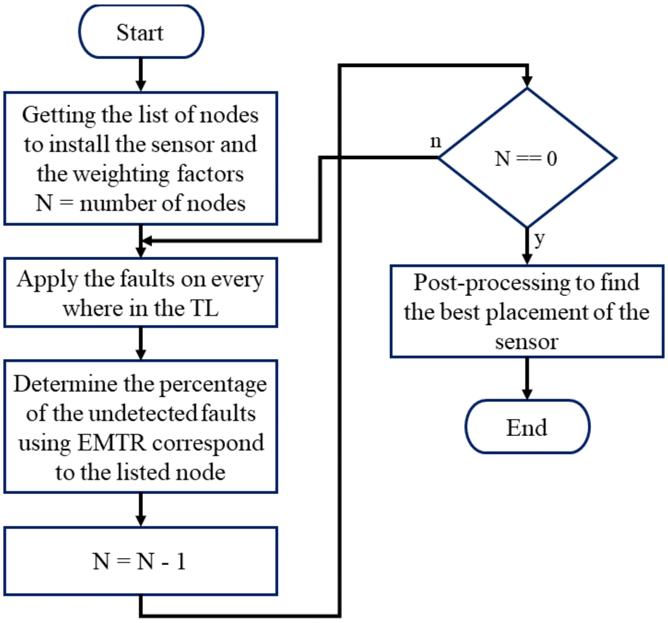

Fig. 7.6 The flowchart of the proposed algorithm.

In this work, we propose to apply a simple algorithm to find the optimal placement of the sensor in the power network. The algorithm is composed of 5 main steps which are detailed in what follows.

1- In the first step, all the possible nodes for the installation of the sensor, N, will be listed. In addition, to account for the economic and /or installation constraints, a weighting factor will be provided for each possible node. The network operator will also specify the desired location accuracy.

2- For each possible node, all the possible fault locations on the power network will be considered and simulated.

3- The EMTR method is applied to locate the faults considered in the previous step. It should be noted here, that in this step, any EMTR-based approach (whether classical or mismatched), with any criteria (energy, cross-correlation, bounded phase, etc.) can be used. The percentage of the faulty nodes that the EMTR method was not able to locate within the considered desired accuracy is calculated.

4- The above steps 2 and 3 are repeated for all the possible locations.

5- Using the percentage of the undetected faults obtained in step 3 and the weighting factor associated with each location, the best placement of the sensor is determined.

The flowchart of the proposed algorithm is shown in Fig. 7.6.

To verify the proposed algorithm to find the optimal placement of the sensor, let us consider the same example as the one considered in Section 7.2 (single-phase network shown in Fig. 7.4). It should be noted that the proposed algorithm can easily be extended to three-phase power networks.

The selected locations to install the sensor for this example are shown using labels Port 1, Port 2 and Port 3 as shown in Fig. 7.4. We applied the proposed algorithm to this network and the results showed that a sensor placed at either of the locations (Port 1, Port 2 or Port 3) can predict all possible faults in the network.

8 Future Works

The proposed EMTR fault location method using the metric of the maximum of the cross-correlation sequence can be further investigated in the following aspects:

- Considering frequency-dependent transmission-line models.
- Application to locate other sources of transients such as direct lightning strike originated flashovers along power networks or conducted intentional electromagnetic interference.

Further research is needed to apply the developed properties and metrics based on EMTR in mismatched media to power networks with more complex topologies.

Another important area of investigation is the identification of fault-originated transients from other types of transients such as those generated by direct and indirect lightning discharges. This identification is needed for the design of an efficient and smart triggering of the measurement system.

Furthermore, the fault location system should be integrated into the SCADA system to satisfy two important requirements, namely (1) to communicate to the power utilities the fault location, and (2) to receive the information on the status of power network switches so that the fault location system can access the real-time topology of the network.

Finally, the application of the EMTR-based methods to High-Voltage (HV) networks would be particularly interesting. However, further studies and research are needed to verify their practical adaptability to HV grids. From an implementation point of view, with reference to the prototype installed at Groupe E and described in Section 4.1 of this report, it is necessary to adapt the sensing unit and consider large-bandwidth sensors suitable for high voltage networks, which currently are not available on the market. From a scientific point of view, two aspects must be considered, i.e. the applicability of the method and the network model. Indeed, it is necessary to verify that the peculiarities of high voltage lines do not invalidate the method itself (e.g., the higher degree of homogeneity of the lines or the possible signal attenuation due to the greater line length compared to MV lines), and at the same time, the network model should be carefully studied to be able to correctly represent all phenomena taking place on HV transmission grids with their timing.

9 Publications

H. Karami, A. Mostajabi, M. Azadifar, Z. Wang, M. Rubinstein, F. Rachidi, "Locating Lightning Using Electromagnetic Time Reversal: Application of the Minimum Entropy Criterion", 2019 International Symposium on Lightning Protection (XV SIPDA), São Paulo, Brazil, 30th September – 4th October 2019.

Z. Wang, F. Rachidi, M. Paolone, M. Rubinstein, and R. Razzaghi, "A Closed Time-Reversal Cavity for Electromagnetic Waves in Transmission Line Networks," *IEEE Trans. Antennas Propag.*, pp. 1–1, 2020.

Z. Wang, Electromagnetic Time Reversal : Theory, Application to Fault Location in Power Networks and Experimental Validation, PhD thesis, doi: 10.5075/epfl-thesis-7488, EPFL, 2020.

10 References

[1] F. Rachidi, M. Rubinstein, and M. Paolone, Eds., *Electromagnetic Time Reversal Application to Electromagnetic Compatibility and Power Systems*. John Wiley & Sons, 2017.

[2] M. Fink, G. Montaldo, and M. Tanter, “Time-Reversal Acoustics in Biomedical Engineering,” *Annual Review of Biomedical Engineering*. 2003.

[3] A. Derode, A. Tourin, J. de Rosny, M. Tanter, S. Yon, and M. Fink, “Taking Advantage of Multiple Scattering to Communicate with Time-Reversal Antennas,” *Phys. Rev. Lett.*, 2003.

[4] A. Tourin, A. Derode, and M. Fink, “Sensitivity to Perturbations of a Time-Reversed Acoustic Wave in a Multiple Scattering Medium,” *Phys. Rev. Lett.*, vol. 87, no. 27, pp. 274301-274301–4, Dec. 2001.

[5] G. F. Edelmann, T. Akal, W. S. Hodgkiss, S. Kim, W. A. Kuperman, and H. C. Song, “An Initial Demonstration of Underwater Acoustic Communication Using Time Reversal,” *IEEE J. Ocean. Eng.*, 2002.

[6] D. Liu, S. Vasudevan, J. Krolik, G. Bal, and L. Carin, “Electromagnetic Time-Reversal Source Localization in Changing Media: Experiment and Analysis,” *IEEE Trans. Antennas Propag.*, 2007.

[7] A. Codino, Z. Wang, R. Razzaghi, M. Paolone, and F. Rachidi, “An Alternative Method for Locating Faults in Transmission Line Networks Based on Time Reversal,” *IEEE Trans. Electromagn. Compat.*, vol. 59, no. 5, pp. 1601–1612, 2017.

[8] G. Lugrin, N. M. Parra, F. Rachidi, M. Rubinstein, and G. Diendorfer, “On The Location of Lightning Discharges Using Time Reversal of Electromagnetic Fields,” *IEEE Trans. Electromagn. Compat.*, vol. 56, no. 1, pp. 149–158, 2014.

[9] N. Mora, F. Rachidi, and M. Rubinstein, “Application of the Time Reversal of Electromagnetic Fields to Locate Lightning Discharges,” *Atmos. Res.*, vol. 117, pp. 78–85, 2012.

[10] S. Y. He *et al.*, “Norm Criteria in the Electromagnetic Time Reversal Technique for Fault Location in Transmission Lines,” *IEEE Trans. Electromagn. Compat.*, vol. 60, no. 5, pp. 1240–1248, 2018.

[11] M. Fink, “Time Reversal of Ultrasonic Fields—Part I: Basic Principles,” *IEEE Trans. Ultrason. Ferroelectr. Freq. Control*, vol. 39, no. 5, pp. 555–566, 1992.

[12] D. Cassereau and M. Fink, “Time-Reversal of Ultrasonic Fields—Part III: Theory of the Closed Time-Reversal Cavity,” *IEEE Trans. Ultrason. Ferroelectr. Freq. Control*, vol. 39, no. 5, pp. 579–592, 1992.

[13] F. Wu, J.-L. Thomas, and M. Fink, “Time Reversal of Ultrasonic Fields---Part II Experimental Results,” *Nucl. Phys.*, vol. 39, no. 5, pp. 567–578, 1992.

[14] Z. Wang, F. Rachidi, M. Paolone, M. Rubinstein, and R. Razzaghi, “A Closed Time-Reversal Cavity for Electromagnetic Waves in Transmission Line Networks,” *IEEE Trans. Antennas Propag.*, pp. 1–1, 2020.

[15] R. Razzaghi, G. Lugrin, H. Manesh, C. Romero, M. Paolone, and F. Rachidi, “An Efficient Method Based on the Electromagnetic Time Reversal to Locate Faults in Power Networks,” *IEEE Trans. Power Deliv.*, vol. 28, no. 3, pp. 1663–1673, 2013.

[16] Z. Wang *et al.*, “Time Reversal Focusing Property in Mismatched Media,” in *2018 American Electromagnetics Conference*, 2018, pp. 1–7.

[17] Z. Chen, Z. Wang, M. Paolone, and F. Rachidi, "Properties of Direct-Time and Reversed-Time Transfer Functions to Locate Disturbances along Power Transmission Lines," in *2019 IEEE PowerTech*, 2019, pp. 1–6.

[18] Z. Wang, "Electromagnetic Time Reversal : Theory, Application to Fault Location in Power Networks and Experimental Validation," 2020.

[19] Z. Wang, R. Razzaghi, M. Paolone, and F. Rachidi, "Electromagnetic Time Reversal Applied to Fault Location: On the Properties of Back-Injected Signals," in *20th Power Systems Computation Conference, PSCC 2018*, 2018, pp. 1–7.

[20] Z. Wang, R. Razzaghi, M. Paolone, and F. Rachidi, "Electromagnetic Time Reversal Similarity Characteristics and Its Application to Locating Faults in Power Networks," *IEEE Trans. Power Deliv.*, vol. 35, no. 4, pp. 1735–1748, 2020.

[21] A. Greenwood, *Electrical Transients in Power Systems*. John Wiley & Sons, 1991.

[22] Z. Wang, R. Razzaghi, M. Paolone, and F. Rachidi, "Time Reversal Applied to Fault Location in Power Networks Pilot Test: Results and Analyses," *Int. J. Electr. Power Energy Syst.*, vol. 114, no. April 2019, p. 105382, 2020.